Monthly Notices of the ROYAL ASTRONOMICAL SOCIETY

MNRAS **536,** 3401–3420 (2025) https://doi.org/10.1093/mnras/stae2803
Advance Access publication 2024 December 23

ExoMol line lists – LXI. A trihybrid line list for rovibronic transitions of the hydroxyl radical (OH)

Georgi B. Mitev, Charles A. Bowesman, Jingxin Zhang, Sergei N. Yurchenko and Jonathan Tennyson★

Department of Physics and Astronomy, University College London, Gower Street, London WC1E 6BT, UK

Accepted 2024 December 18. Received 2024 December 18; in original form 2024 November 7

ABSTRACT

The hydroxyl radical (OH) is a species of high importance in exoplanetary studies, the interstellar medium, and in stellar spectra. Terrestrially, it is a significant component of combustion chemistry, an oxidizer in the upper atmosphere, and a source of telluric bands. Internally contracted multireference configuration interaction potential energy curves, spin-orbit couplings, electronic angular momentum couplings, and (transition) dipole moments for eight electronic states of OH are computed and refined against empirical energy levels to produce an OH spectroscopic model. A line list consisting of rovibronic term values, allowed electronic dipole transitions, Einstein-A coefficients, and partition functions for varying temperature and a continuum absorption data set are then produced by variational solution of the coupled-channel Schrödinger equations using the nuclear motion code DUO. MARVEL energy levels substitute equivalent levels in the OH line list, with estimated uncertainties in experimentally dark regions, following an established hybridization procedure. Predissociation lifetimes of the A $^2\Sigma^+$ state are calculated using a stabilization method and convoluted with natural lifetimes to include predissociative effects. Continuum absorption cross-sections for $T \in [100, 200, ..., 8000]$ K and zero pressure are provided in the range of $0 \rightarrow 80\,000\,\mathrm{cm}^{-1}$ with a step size of $0.01\,\mathrm{cm}^{-1}$. Comparison with available literature cross-sections exhibits strong agreement. The line list is suitable for high-resolution studies up to 8000 K. The OH MYTHOS data set is available for download via www.exomol.com.

Key words: molecular data – Earth – Exoplanets – planets and satellites: atmospheres.

1 INTRODUCTION

The hydroxyl radical, OH, is a molecule of high importance in terrestrial atmospheric chemistry in several contexts, including Meinel band night-glow (Meinel 1950; Chen et al. 2021), which is an important source of heat in the upper atmosphere (Brasseur & Offermann 1986; Kaufmann et al. 2008; Franzen et al. 2019; Chen et al. 2021); due to its role in the lower atmosphere as an oxidizer, especially in reactions with ozone-depleting CFCs (Prinn et al. 1995), and for its interactions with aromatic molecules such as benzene and toluene (Garmash et al. 2020).

OH has been detected in many planets and exoplanets including Venus (Piccioni et al. 2008), Mars (Clancy et al. 2013) and ultrahot Jupiters Wasp-76b (Landman et al. 2021), and Wasp-33b (Nugroho et al. 2021). Further detections have been made in the interstellar medium (Weinreb et al. 1963; Zannese et al. 2023), in protoplanetary discs at moderate temperatures (Munoz-Romero et al. 2024), and in stellar environments such as M-dwarfs (Herbig 1974; Jones et al. 1988) and sunspots (Berdyugina & Solanki 2001).

Many of the early theoretical studies of hydroxyl spectroscopy were performed by van Dishoeck and Langhoff et al., computing potential energy curves (PECs) for many electronic states, their dipoles, transition spectra, predissociation spectra, and photodissociation spectra (Langhoff et al. 1982; van Dishoeck & Dalgarno 1983; van Dishoeck, Langhoff & Dalgarno 1983; van Dishoeck et al. 1984; van Dishoeck & Dalgarno 1984a; van Dishoeck & Dalgarno 1984b; Bauschlicher & Langhoff 1987), which form the base of the photoabsorption spectrum given by the Leiden database (Hrodmarsson & van Dishoeck 2023). Recent theoretical studies into the electronic structure of OH have been performed by Srivastava & Sathyamurthy (2014), Qin & Zhang (2014), and most notably by van der Loo & Groenenboom (2005), which inform most of the electronic structure calculations performed in this paper.

Hydroxyl has seen much experimental and empirical spectroscopic study, including, but not limited to studies by Colin et al. (2002), Bernath & Colin (2009), Brooke et al. (2016), Yousefi et al. (2018), Coxon, Sappey & Copeland (1991), Sulakshina & Borkov (2023), with those by Brooke et al. (2016) and Yousefi et al. (2018) appearing to make up a majority if not all of the current HITRAN line list (Gordon et al. 2022). Recently Furtenbacher et al. (2022) released a MARVEL data set of energy levels which are used extensively here (Section 1.1).

This paper covers the formation of a replacement to the current ExoMol line list for OH. The current line list is based on the works by Brooke et al. (2016) and Yousefi et al. (2018) (MOLLIST, Bernath 2020), similar to the current HITRAN line list. The motivation behind improving the line list, in addition to the general atmospheric and

---

★ E-mail: j.tennyson@ucl.ac.uk

Table 1. Summary of all electronic states of OH considered in the $^{16}O^{1}H$MYTHOS line list and their use case.

State	Line list	Predissociation widths	Continuum absorption
X $^2\Pi$	✓		✓
A $^2\Sigma^+$	✓	✓	✓
^{a}B $^2\Sigma^+$	✓	✓	✓
^{a}C $^2\Sigma^+$	✓	✓	
1 $^2\Sigma^-$		✓	✓
1 $^4\Sigma^-$		✓	
1 $^4\Pi$		✓	
1 $^2\Delta$			✓

[a] Predissociation widths are not rigorously calculated for these states, however, the all levels in these states are assumed to be dissociative due to crossings with local repulsive states, as such, are included in line list with predissociation widths equal to their natural width.

astrophysical interest in OH, is that the MoLLIST data set does not currently consider dissociative processes, such as predissociation and continuum absorption, which are important sources of opacity in many astrophysical environments. Furthermore, the MoLLIST line list's intensities in the Meinel bands have recently seen criticism by Medvedev, Ermilov & Ushakov (2024), as intensities appear to be unphysical past $\Delta v = 5$. Lastly, this update gives the opportunity to leverage the aforementioned MARVEL data set to extend the line list to include two additional bound electronic states, B $^2\Sigma^+$ and C $^2\Sigma^+$, whereas MoLLIST contains only X $^2\Pi$ and A $^2\Sigma^+$. This new line list we call MYTHOS.

This project starts with the computation of new *ab initio* PECs and their corresponding diagonal and off-diagonal coupling curves for the electronic states mentioned in Table 1. These calculations are very much based on the work by van der Loo & Groenenboom (2005) and are described in Section 2. The process of further refining these curves and forming the spectroscopic model used to produce the bound–bound line list is discussed in Section 3, with further discussion into the isolation of bound–bound transitions in Section 4.

The initial study of OH within ExoMol was focused on the computation of predissociation lifetimes of the A $^2\Sigma^+$ state, leveraging a five-state spectroscopic model containing the X $^2\Pi$, A $^2\Sigma^+$, and 1 ($^2\Sigma^-$,^{4} Σ^-,^{4} Π) states (see Mitev, Yurchenko & Tennyson, 2024, hereafter referred to as Paper I). This returned accurate predissociation widths which are used to inform the lifetime broadening parameters used for the A$^2\Sigma^+$ $\leftarrow$ X$^2\Pi$ transition spectrum. Since this work, the X $^2\Pi$ and A $^2\Sigma^+$ state curves have been updated, as such the methods outlined in Paper I have been repeated to produce new predissociation lifetimes which are made available in the supplementary material. A description of the simulation of the absorption spectra of OH including the dissociation effects is given in Section 5 with final results including sample spectra produced in Section 6.

1.1 Summary of MARVEL energies and quantum number conventions

Furtenbacher et al. (2022) collected 15938 rovibronic transitions from 45 sources and produced values for 1619 empirical rovibronic energy levels for the system of electronic states, X $^2\Pi$, A $^2\Sigma^+$, B $^2\Sigma^+$, C $^2\Sigma^+$. Table 2 summarizes the coverage of the MARVEL energy levels used in this study.

Table 2. Coverage of MARVEL data set (Furtenbacher et al. 2022) energy levels for the X $^2\Pi$, A $^2\Sigma^+$, B $^2\Sigma^+$, and C $^2\Sigma^+$ states of OH which have been used to refine *ab initio* PECs, SOCs and coupling constants for the production of a spectroscopic model.

v	$J_{\rm min}$	$J_{\rm max}$	Number of levels
	X $^2\Pi$		
0	0.5	49.5	196
1	0.5	42.5	154
2	0.5	41.5	152
3	0.5	36.5	131
4	0.5	19.5	77
5	0.5	19.5	76
6	0.5	18.5	74
7	0.5	18.5	74
8	0.5	18.5	74
9	0.5	18.5	74
10	0.5	11.5	42
11	0.5	8.5	23
12	0.5	7.5	28
13	0.5	7.5	27
Total	0.5	49.5	1202
	A $^2\Sigma^+$		
0	0.5	36.5	73
1	0.5	28.5	58
2	0.5	19.5	40
3	0.5	26.5	54
4	0.5	19.5	40
5	0.5	7.5	15
6	0.5	8.5	17
7	0.5	7.5	16
8	0.5	9.5	19
9	0.5	8.5	17
Total	0.5	36.5	349
	B $^2\Sigma^+$		
0	0.5	10.5	21
1	0.5	8.5	17
Total	0.5	10.5	38
	C $^2\Sigma^+$		
0	0.5	7.5	15
1	0.5	7.5	15
Total	0.5	7.5	30
Grand total	0.5	49.5	1619

The complete set of quantum numbers used to characterize the MARVEL energy levels are the state label (X $^2\Pi$, A $^2\Sigma^+$, 1 $^2\Sigma^-$,...) total angular momentum, J, the vibrational quantum number, v, the rotationaless parity, e/f, and the projection of the total angular momentum on the molecular axis, $\Omega = \Sigma + \Lambda$, where, Σ and Λ are projections of the spin and orbital angular momenta on the molecular axis, respectively.

In line with the Hund's case (a) conventions used in DUO, the following quantum numbers are used to characterize the rovibronic states, $|J,\ v,\ \tau,\ \Sigma,\ \Lambda,\ \Omega,\ \text{state}\rangle$ where state is a counting number associated with the electronic states as ordered by potential minima, $T_{\rm e}$, and τ is the state parity $+/-$ (see Tennyson et al. 2016 for conversion between e/f and τ), which can be directly related to the MARVEL data set.

Instead of using the Hund's case (a) convention, many data sets on the rovibronic state of OH in the literature opt for the rotational quantum number N and the fine-structure components, F_1 and F_2 (Hund's case b). In order to correlate these data with our MARVEL data set, their representations have been converted into the rigorous quantum labels J, e/f using the following relations.

For the $^2\Sigma^+$ states:

$$J = \begin{cases} N + \dfrac{1}{2} & \text{for } F_1 \\ N - \dfrac{1}{2} & \text{for } F_2, \end{cases} \tag{1}$$

$$e/f = \begin{cases} f & \text{for } F_1 \\ e & \text{for } F_2. \end{cases} \tag{2}$$

These relations arise, in particular, as the (A, B, C) $^2\Sigma^+$ state levels are generally presented using Hund's case (b), hence the relation between J and N, equation (1) and due to the common approximation,

$$E_{F_1} = BN(N+1) + \frac{1}{2}\gamma N, \tag{3}$$

$$E_{F_2} = BN(N+1) - \frac{1}{2}\gamma (N+1). \tag{4}$$

Therefore, because $\gamma \ll B$, (Brooke et al. 2016) where B is the rotational constant and γ is the spin-rotation constant,

$$E_{F_1} > E_{F_2} \;\; \forall \;\; N, J \tag{5}$$

and since the $^2\Sigma^+$ states have only parity splitting as $\Lambda^{^2\Sigma^+} = 0$, the F_1 and F_2 components correspond directly to f and e parities, respectively (for a given J) (Herzberg 1989).

For the X $^2\Pi$ state the relevant Hund's case (a) approximation is

$$E_{F_1} = B[(J+S)^2 - \Lambda^2] - \frac{1}{2}(A - 2B), \tag{6}$$

$$E_{F_2} = B[(J+S)^2 - \Lambda^2] + \frac{1}{2}(A - 2B), \tag{7}$$

where A is the diagonal spin-orbit coupling. This is applied for a given parity and correlates with the following relation (Herzberg 1989):

$$E_{F_1} = E\left(\Omega = \frac{3}{2}\right) < E_{F_2}, \tag{8}$$

$$E_{F_2} = E\left(\Omega = \frac{1}{2}\right) > E_{F_1}. \tag{9}$$

The quantum number correlations for the quartet 1 ($^4\Sigma^-$,$^4\Pi$,$^2\Delta$) states have not been considered here as there are no experimental data which will require transformation.

2 METHODS: ELECTRONIC STRUCTURE CALCULATIONS

Initial electronic structure calculations were performed for the X $^2\Pi$, A $^2\Sigma^+$, and 1 ($^2\Sigma^-$,$^4\Sigma^-$,$^4\Pi$) electronic states as part of a study into the predissociation dynamics of the A $^2\Sigma^+$ state in Paper I. Following this, further calculations were performed to study the B $^2\Sigma^+$, C $^2\Sigma^+$, and 1 $^2\Delta$ states of OH as part of this line list. In line with this development, this section is divided into two subsections. Section 2.1 covers the calculations pertaining to the X $^2\Pi$, A $^2\Sigma^+$, and 1 ($^2\Sigma^-$,$^4\Sigma^-$,$^4\Pi$) electronic states and Section 2.2 builds on this work, extending it to the B $^2\Sigma^+$, C $^2\Sigma^+$, and 1 $^2\Delta$ electronic states.

2.1 X $^2\Pi$, A $^2\Sigma^+$ and 1 ($^2\Sigma^-$,$^4\Sigma^-$,$^4\Pi$)

Table 3. Summary of *ab initio* electronic structure calculation details. All calculations use aug-cc-pV6Z basis set with the first σ orbital closed. Orbitals correspond to the point group symmetry C_{2v}.

Curve	SA-CASSCF	Space
PECs		
X $^2\Pi$	X $^2\Pi_x$, X $^2\Pi_y$	$5\sigma 2\pi$
A $^2\Sigma^+$, 1 $^2\Sigma^-$	A $^2\Sigma^+$, 1 $^2\Sigma^-$	$5\sigma 2\pi$
1 $^4\Sigma^-$	A $^2\Sigma^+$, 1 $^2\Sigma^-$, 1 $^4\Sigma^-$	$5\sigma 2\pi$
1 $^4\Pi$	1 $^4\Pi_x$,1 $^4\Pi_y$, A $^2\Sigma^+$	$6\sigma 2\pi$
Coupling curves		
$\langle$X $^2\Pi \vert \hat{H}_{SO} \vert$A $^2\Sigma^+\rangle$	X $^2\Pi_x$, X $^2\Pi_y$, A $^2\Sigma^+$	$5\sigma 2\pi$
$\langle$X $^2\Pi \vert \hat{L}_x \vert$A $^2\Sigma^+\rangle$	X $^2\Pi_x$, X $^2\Pi_y$, A $^2\Sigma^+$	$5\sigma 2\pi$
$\langle$X $^2\Pi \vert \hat{H}_{SO} \vert$X $^2\Pi\rangle$	X $^2\Pi_x$, X $^2\Pi_y$	$5\sigma 2\pi$
$\langle$A $^2\Sigma^+ \vert \hat{H}_{SO} \vert$1 $^2\Sigma^-\rangle$	A $^2\Sigma^+$, 1 $^2\Sigma^-$	$5\sigma 2\pi$
$\langle$A $^2\Sigma^+ \vert \hat{H}_{SO} \vert$1 $^4\Sigma^-\rangle$	A $^2\Sigma^+$, 1 $^2\Sigma^-$, 1 $^4\Sigma^-$	$5\sigma 2\pi$
$\langle$A $^2\Sigma^+ \vert \hat{H}_{SO} \vert$1 $^4\Pi\rangle$	1 $^4\Pi_x$,1 $^4\Pi_y$, A $^2\Sigma^+$	$6\sigma 2\pi$
(Transition) dipole moments		
$\langle$X $^2\Pi \vert \hat{\mu}_z \vert$X $^2\Pi\rangle$	X $^2\Pi_x$, X $^2\Pi_y$	$5\sigma 2\pi$
$\langle$A $^2\Sigma^+ \vert \hat{\mu}_z \vert$A $^2\Sigma^+\rangle$	A $^2\Sigma^+$, 1 $^2\Sigma^-$	$5\sigma 2\pi$
$\langle$X $^2\Pi \vert \hat{\mu}_x \vert$A $^2\Sigma^+\rangle$	X $^2\Pi_x$, X $^2\Pi_y$, A $^2\Sigma^+$	$5\sigma 2\pi$
$\langle$X $^2\Pi \vert \hat{\mu}_x \vert$1 $^2\Sigma^-\rangle$	X $^2\Pi_x$, X $^2\Pi_y$, A $^2\Sigma^+$, 1 $^2\Sigma^-$	$5\sigma 2\pi$

The initial PECs, spin-orbit coupling curves (SOCs) and angular momentum coupling curves (AMCs) were computed using the MOLPRO quantum chemistry program (Werner et al. 2010, 2012, 2020). Following van der Loo & Groenenboom (2005), optimal molecular orbitals were computed using carefully selected combinations of state-averaged complete active space self-consistent field (SA-CASSCF) (Werner & Knowles 1985) calculations: details of which are given in Table 3. These orbitals provide the input to multireference configuration interaction (MRCI) calculations which included a Davidson correction (Langhoff & Davidson 1974) to the energies. Final results were computed using an aug-cc-pV6Z basis set. The calculations were performed over internuclear distances ranging from 1 to 10a_0 with a greater density of points around the equilibrium bond length. We ensured that no $^2\Delta$ states were obfuscating the presence of the desired $^2\Sigma^\pm$ states by calculating PECs for both A_1 and A_2 irreducible representations of C_{2v} and selecting the appropriate symmetries.

MOLPRO produces coupling curves and dipoles with an arbitrary phase factor of ±1 or $\pm i$ which is not guaranteed consistent between geometries. This uncertainty in phase leads to discontinuities in the curves and hence requires post-processing. Within an MRCI calculation informed by a set of SA-CASSCF orbitals, the phase may not be consistent between geometries, however, it is consistent over all curves computed with those orbitals for a given geometry; any discontinuities will appear in the same places for all curves (Patrascu et al. 2014). The coupling curves in this study, however, were not all computed with one set of orbitals and instead were split up as shown in the SA-CASSCF column in Table 3. Inter-SA-CASSCF phase consistency was ensured by first smoothing all curves with an arbitrary global phase and comparing to a set of reference curves. These were produced by performing an aug-cc-pVTZ calculation with all states present in the SA-CASSCF, ensuring phase consistency between all relevant curves.

The reference curve calculation covers all curves initially computed with the aug-cc-pV6Z. As all curves in the TZ calculation are computed with the same SA-CASSCF, they are phase consistent with each other for a given geometry. In principle, these curves would still require smoothing to remove discontinuities, and if this is to be done, it must be ensured that all phase changes are applied consistently. In this work, all curves came out smooth from MOLPRO and no such

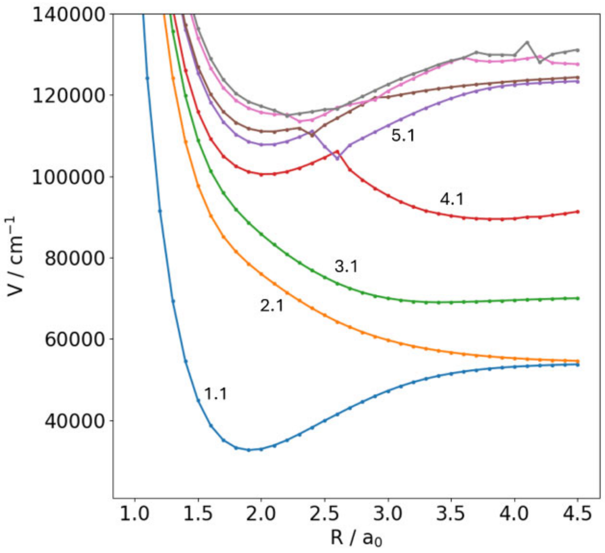

Figure 1. First eight A_1 symmetry PECs of OH as calculated in MOLPRO using the aug-cc-pV5Z basis set and $6\sigma 2\pi$ active space.

smoothing was required. After this calculation, the 6Z curves' phases are matched to that of the reference curves to retrieve the final results.

2.2 (B,C) $^2\Sigma^+$ and 1 $^2\Delta$

The curves pertaining to the B $^2\Sigma^+$, C $^2\Sigma^+$, and 1 $^2\Delta$ states were computed similarly as the others as described above. These states have A_1 irreducible representation in C_{2v} point group symmetry.

The 1 $^2\Delta$ state has the degenerate A_1/A_2 representation. To identify this state, calculations including both representations were performed. The PEC corresponding to the 1 $^2\Delta$ state was found to be degenerate in these representations, as expected, and so could be identified. Results were compared with the curves of van der Loo & Groenenboom (2005) to verify the shape and asymptotic energy of the potential.

B $^2\Sigma^+$ was identified similarly by checking against the asymptotic limits. It is expected that the energy gap between the A $^2\Sigma^+$ and B $^2\Sigma^+$ asymptotic limits should be of the order of 18 000 cm^{-1} (Kramida et al. 2021) as the A $^2\Sigma^+$ state tends to the O(^{1}D) + H(^{2}S) atomic limit and the B $^2\Sigma^+$ state tends to the O(^1S) + H(^{2}S) atomic limit. This was found to be the case and the shape of the curve was again verified against van der Loo & Groenenboom (2005).

A difficulty in this calculation was identifying the C $^2\Sigma^+$ state, especially since many states were required in the SA-CASSCF to achieve convergence. In this calculation, the A $^2\Sigma^+$, 1 $^2\Delta$, B $^2\Sigma^+$, and C $^2\Sigma^+$ states were present, along with a further four A_1 states, which have not been used in the production of the spectroscopic model. The C $^2\Sigma^+$ state exhibited orbital swapping and avoided crossings with the other local states. This is visible in Fig. 1; PECs are labelled [E].[S], where [E] is the energy ordering label, and [S] is the irreducible representation in C_{2v} where $[S] = 1, 2, 3, 4 = A_1, B_1, B_2, A_2$, respectively. The C $^2\Sigma^+$ state was identified by its characteristically high equilibrium bond length at $\sim 3.8\ a_0$ as was shown by Langhoff et al. (1982).

From this, it can be seen that, the third and fourth PECs correspond to B $^2\Sigma^+$ and C $^2\Sigma^+$ electronic states. The C $^2\Sigma^+$ *ab initio* PEC (4.1) is problematic, however, as the short-range PEC is tangled with high-energy Rydberg states. Untangling the swapped orbitals and dealing with avoided crossings was deemed impractical and unproductive.

Table 4. Mapping between dipoles and numerical representation of A_1 states in MOLPRO for OH.

Dipole	Numerical representation
$\langle \mathrm{X}\ ^2\Pi \vert \hat{\mu}_x \vert 1\ ^2\Delta \rangle$	$\langle 1.2 \vert \hat{\mu} \vert 2.1 \rangle$
$\langle \mathrm{X}\ ^2\Pi \vert \hat{\mu}_x \vert \mathrm{B}\ ^2\Sigma^+ \rangle$	$\langle 1.2 \vert \hat{\mu} \vert 3.1 \rangle$
$\langle \mathrm{X}\ ^2\Pi \vert \hat{\mu}_x \vert \mathrm{C}\ ^2\Sigma^+ \rangle$	$\langle 1.2 \vert \hat{\mu} \vert 4.1 \rangle$

Table 5. Details of MOLPRO calculation for the B $^2\Sigma^+$, C $^2\Sigma^+$, and 1 $^2\Delta$ electronic states of OH all with an active space of $6\sigma 2\pi$.

Curve	SA-CASSCF	Basis set
PECs		
B $^2\Sigma^+$, C $^2\Sigma^+$, 1 $^2\Delta$	(A, B, C) $^2\Sigma^+$, 1 $^2\Delta$, + 4A_1	aug-cc-pV6Z
(T)DMCs		
$\langle \mathrm{X}\ ^2\Pi \vert \hat{\mu}_x \vert \mathrm{B}\ ^2\Sigma^+ \rangle$	(A, B, C) $^2\Sigma^+$, 1 $^2\Delta$, + 4A_1	aug-cc-pV5Z
$\langle \mathrm{X}\ ^2\Pi \vert \hat{\mu}_x \vert \mathrm{C}\ ^2\Sigma^+ \rangle$	(A, B, C) $^2\Sigma^+$, 1 $^2\Delta$, + 4A_1	aug-cc-pV5Z
$\langle \mathrm{X}\ ^2\Pi \vert \hat{\mu}_x \vert 1\ ^2\Delta \rangle$	(A, B, C) $^2\Sigma^+$, 1 $^2\Delta$, + 4A_1	aug-cc-pV5Z

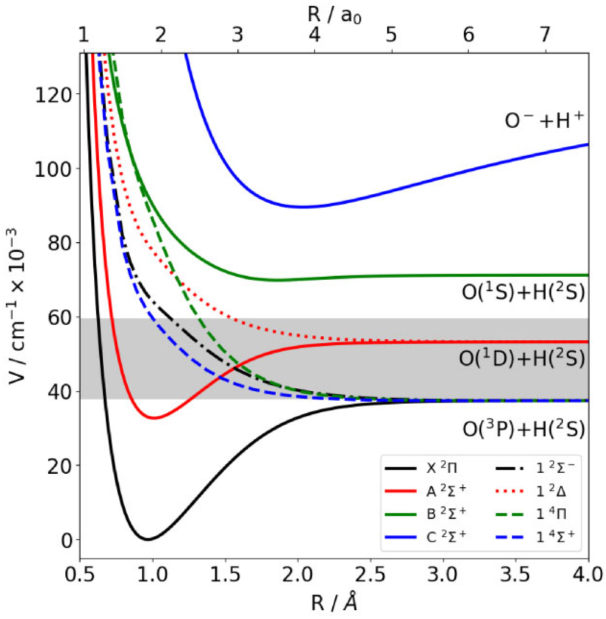

Figure 2. PECs used in the spectroscopic model of OH. Solid lines: bound–bound line list, dashed lines: predissociative broadening only, dotted lines: continuum absorption only, dotted + dashed: continuum absorption + predissociative broadening. The shaded area contains all A $^2\Sigma^+$ rovibronic levels with predissociative broadening.

Instead, this PEC was used to extract a rough guide for the potential minimum, T_e.

We find from Fig. 1 that the relevant dipoles correspond to the numerical symmetry representations from MOLPRO as in Table 4. These mappings were used when calculating the (transition) dipole moment curves for these electronic states. Details of these calculations are given in Table 5.

Visual representations of the PECs, SOCs, and EAMC considered in this section are made available in Figs 2, 3, and 4, respectively. Further discussion on the (transition) dipole moment curves is given in Section 6.1.2.

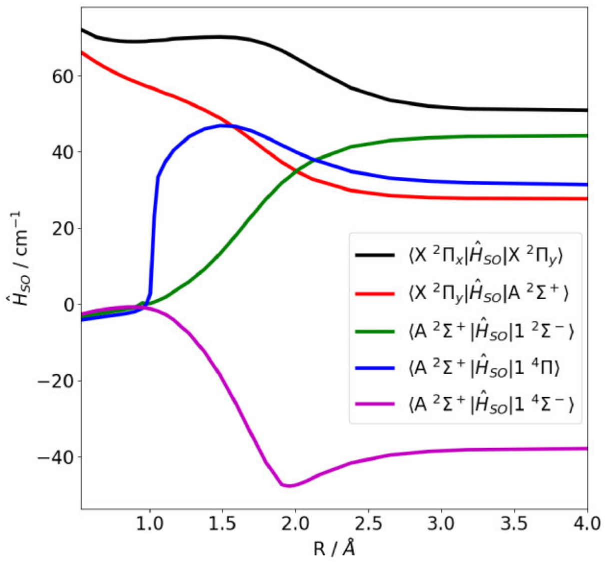

Figure 3. Diagonal and off-diagonal *ab initio* SOCs of OH as computed in MOLPRO. The curves here also have an associated factor of $\pm i$.

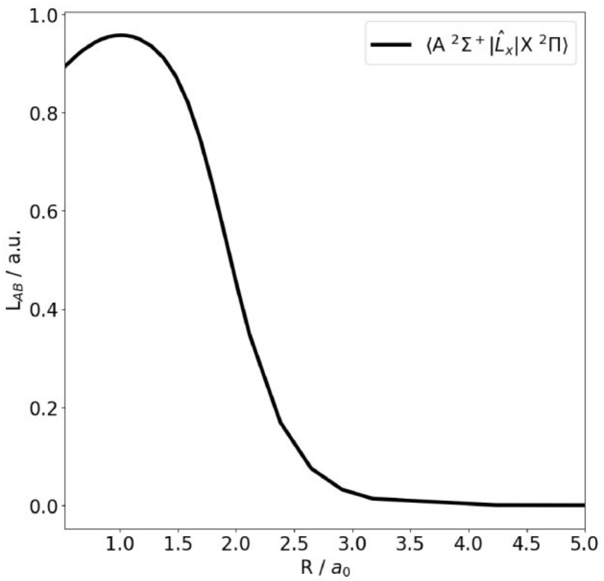

Figure 4. *Ab initio* L-uncoupling matrix elements for OH as computed in MOLPRO. In the Cartesian coordinate system, there is a factor of $\pm i$.

3 METHODS: SPECTROSCOPIC MODEL AND LINE LIST

The aforementioned set of *ab initio* curves can be used as input to the nuclear motion code DUO (Yurchenko et al. 2016), an open-source FORTRAN 2009 program which provides variational solutions to the coupled rovibronic Schrödinger equations for a general open-shell diatomic molecule, obtaining rovibrational energies and transitions.

Typically, even when a high level of electronic structure theory is employed, *ab initio* curves are insufficient for adequate modelling of rovibronic energy structure. This, indeed is the most important factor for errors in rovibronic energy calculations. Further to this, experimental energy levels include all possible PECs and couplings implicitly. In principle, one could improve the accuracy of the *ab initio* model by raising the level of theory used for the initial calculations and improve the treatment of the couplings by computing an increasing number of curves with the same high level of theory. In practice, however, this is not always feasible. In particular, with increasing energy, the density of electronic states increases, making PECs and couplings more challenging to compute. Moreover, basis functions associated with continuum states can play a large role in the rovibronic energies of bound states (see e.g. Kozlov, Pazyuk & Stolyarov 2024). Here, the electronic structure calculations are limited to a selected number of states and associated couplings, meaning that whatever effects additional states would have on the term values is rerouted through refining the available PECs, coupling curves, and empirical parameters.

Three flavours of curve refinement are available in DUO, parameter variation of an analytic representation (hereafter referred to simply as parameter variation), morphing (Meuwly & Hutson 1999; Skokov, Peterson & Bowman 1999; Patrascu et al. 2014), and grid-point variation. Independent of the type of refinement, the curves are iteratively modified by solving the nuclear motion problem and comparing the rovibronic levels or transitions with experimentally derived values. These are often given in the form of MARVEL data sets (Section 1.1) or in the form of molecular constants which are then converted to energy levels using an effective Hamiltonian code such as PGOPHER (Western 2017). At each iteration, a conjugate gradient descent algorithm is applied to compute new curve shapes until a weighted least-squares solution to the nuclear motion problem is found. In this work, parameter variation and morphing are used and are described briefly as follows.

Parameter variation works by first assigning an analytic form to the curve in question and then varying the parameters through the procedure described above. For PECs, the analytic forms used in this study are the extended Morse potential (Section 3.2) (Lee et al. 1999; Le Roy, Huang & Jary 2006), and the Morse long-range potential (MLR, Section 3.3, Le Roy et al. 2006, 2009, 2011; Le Roy & Henderson 2007). Common between them are the parameters which describe the primary features of a PEC, those being the position of the potential minimum, T_e, the asymptotic energy limit, the dissociation limit relative to the ground electronic state potential minimum, D_e, and the equilibrium bond length, R_e. The remaining parameters further refine the shape of the potential, making it narrower, wider, or adjusting the shape of the long-range region at internuclear separations greater than R_e. This type of refinement is typically only performed on PECs as it is necessary to know R_e, T_e, and D_e when comparing to literature and coupling curves do not have a standard set of analytic forms which are easy to implement.

In the case of couplings, morphing is more applicable. Morphing is similar to parameter variation fitting with one degree of separation. In this case, one does not vary the curve in question directly, but instead varies the parameters describing a morphing function, $f_m(R)$, which, in turn, scales the *ab initio* curve, $f_{ai}(R)$:

$$f_{\text{morphed}}(R) = f_{\text{ai}}(R) f_{\text{m}}(R). \quad (10)$$

This is not typically applied when refining PECs as it then becomes difficult or impossible to arrive at accurate reproduction of the equilibrium bond length, R_e, directly from the morphing form, which is a parameter of interest. The form of morphing used here is due to Meuwly & Hutson (1999) and has the drawback that scaling a function will not alter its value at points where the original function is zero; the alternative morphing approach due to Skokov et al. (1999) scales the coordinate not the function which means that these zero values can be shifted if not removed. The form given in equation (10) proved to be satisfactory for the current study.

3.1 Global parameters

DUO uses an initial grid in a sinc-DVR (discrete variable representation) which gives evenly spaced grid points over a user-specified finite region. A $J = 0$ problem is then solved for each PEC (with all couplings neglected) to provide a set of vibrational basis functions for each state. This means that a number of global parameters need to be established before running a DUO calculation, they are as follows: the size of vibrational basis sets ($\upsilon_{\max}$) for each electronic state, the start ($R_{\min}$) and end ($R_{\rm c}$) of the calculation box, the number of grid points, and the maximum value for J. These considerations are made to ensure converged solutions for the energy levels. The start and end of the box was set to 0.53 and 8 Å, respectively, with a grid size of 801 points.

The value of $\upsilon_{\max}$ was selected for each electronic state iteratively. By extracting energy eigenvalues within the relevant fitting region (defined by the quantum number coverage of Table 2) for increasing $\upsilon_{\max}$, we can set $\upsilon_{\max}$ such that the energy levels are converged. This was found to occur when $\upsilon^{\rm X}_{\max} \geq 110$ and $\upsilon^{\rm A}_{\max} \geq 90$. The size of the vibrational basis sets were hence set to 110 and 90 for the X $^2\Pi$ and A $^2\Sigma^+$ states, respectively. This procedure was repeated for the B $^2\Sigma^+$ and C $^2\Sigma^+$ states and it was found that $\upsilon^{\rm B,C}_{\max} \geq 10$ was sufficient. The maximum value for J, $J_{\max}$, was set to 49.5.

3.2 Fitting – X $^2\Pi$ and A $^2\Sigma^+$

The PECs and coupling curves were refined by making constrained adjustments to parameters which describe them with respect to a set of observed data, which can be of empirical energy levels or transitions. These data are supplied by the recent MARVEL data set's energy levels (Furtenbacher et al. 2022). Curve refinement is performed in DUO by least-squares fitting to this data set. As stated earlier, DUO provides three types of fitting one can use: variation of parameters that describe a curve (Section 3.2.1), variation of parameters that describe a morphing function (*morphing*, see Section 3.2.2), and direct variation of individual grid points. In each case, the optimization is based on a non-linear conjugate gradient method (Yurchenko et al. 2016) with respect to an empirical data set.

3.2.1 Parameter variation fitting – *pre-fitting*

During parameter variation fitting, the curves must have some parametric form, and some initial set of parameters must be determined. For PECs, the form used for the X $^2\Pi$ and A $^2\Sigma^+$ states is the extended Morse oscillator (EMO) (Lee et al. 1999; Le Roy et al. 2006; Yurchenko et al. 2016; Le Roy 2017), given by

$$V_{\rm EMO}(R) = T_{\rm e} + (A_{\rm e} - T_{\rm e})\left(1 - {\rm e}^{-\beta(R)(R-R_{\rm e})}\right)^2, \tag{11}$$

where $T_{\rm e}$ is the potential minimum, $D_{\rm e} = A_{\rm e} - T_{\rm e}$ is the dissociation energy relative to $T_{\rm e}$, $A_{\rm e}$ is the dissociation asymptote, $R_{\rm e}$ is the equilibrium bond length, and $\beta(R)$ is a distance-dependent exponent coefficient defined by the expansion term with coefficients β_i with respect to the reduced coordinate ξ_p, first introduced by Šurkus, Rakauskas & Bolotin (1984) and are given by

$$\beta(R) = \sum_{i=0}^{N} \beta_i \xi_p(R)^i; \quad N = \begin{cases} N_R & \text{for } R > R_{\rm e} \\ N_L & \text{for } R \leq R_{\rm e}, \end{cases} \tag{12}$$

$$\xi_p(R) = \frac{R^p - R_{\rm e}^p}{R^p + R_{\rm e}^p}; \quad p = \begin{cases} p_R & \text{for } R > R_{\rm e} \\ p_L & \text{for } R \leq R_{\rm e}. \end{cases} \tag{13}$$

This parametric form is flexible in that one can specify the behaviour around the equilibrium internuclear distance piece-wise using the parameters N_L, N_R, p_L, and p_R, where $N_L \leq N_R$. The value of N_R hence defines the order of the expansion. This means one can establish a family of PECs where the fundamental shape is determined by the set of parameters, S, (the shape set) where

$$S = \{p_L,\ p_R,\ N_L,\ N_R\};\ \{p_L,\ p_R,\ N_L,\ N_R\} \in \mathbb{Z},\ N_R \geq N_L. \tag{14}$$

Table 6. Summary of the initial shape sets (see Section 3.2.1) for the X $^2\Pi$, A $^2\Sigma^+$, B $^2\Sigma^+$, and C $^2\Sigma^+$ states of OH.

Parameter – EMO	X $^2\Pi$	A $^2\Sigma^+$
p_L	4	3
p_R	3	3
N_L	6	4
N_R	8	8
Parameter – MLR	B $^2\Sigma^+$	C $^2\Sigma^+$
p	2	2
$\beta_{\max}$	3	0
C_n	$C_6 \approx 47\,686.64$ cm^{-1}Å^6	$C_1 \approx 116\,140.93$ cm^{-1} Å

For a given S, one can then find P which refines the shape to return appropriate energy levels, such that:

$$P = \{\beta_i,\ r_{\rm e},\ T_{\rm e},\ D_{\rm e}\};\ \ i \leq N_R. \tag{15}$$

When fitting a PEC in DUO, S is fixed, and hence should be carefully chosen before optimizing P. Initial parameter selection was performed by extending the methods given in Mitev et al. (2022). This problem can be solved iteratively.

The optimization of S is initiated by establishing the set,

$$\sigma_S = \{S_0, ..., S_n\}, \tag{16}$$

$$\equiv \{\{p_{L_0}, p_{R_0}, N_{L_0}, N_{R_0}\}, ..., \{p_{L_n}, p_{R_n}, N_{L_n}, N_{R_n}\}\}, \tag{17}$$

which contains n elements of the set, S, as in equation (14) such that,

$$S_i \neq S_j\ \forall\, i, j;\ \ i \neq j. \tag{18}$$

This is the set of values of p_L, p_R, N_L, and N_R over which we would like to test. The test consists of, for each S_i, finding the conjugate P_i by least-squares fitting against the *ab initio* grid points in PYTHON. In each case, we find the reduced χ^2 test statistic, χ^2_ν and search for the S, P which return the lowest value. These parameters are then used as a starting point for curve refinement of the PECs against experimental data in DUO. See Table 6 for the S parameters for the X $^2\Pi$ and A $^2\Sigma^+$ states in this study.

3.2.2 *Morphing*

For morphing, a *polynomial decay* morphing function of the following form was used:

$$f_{\rm m}(R) = \sum_{k=0}^{N} B_k z^k (1 - \xi_p) + \xi_p B_\infty, \tag{19}$$

where

$$z(r) = (R - R_{\rm ref}){\rm e}^{-\beta(R-R_{\rm ref})^2 - \gamma(R-R_{\rm ref})^4},$$

ξ_p is as in equation (13), B_k are variable expansion coefficients, β and γ are static coefficients typically set to 0.8 and 0.02, respectively, B_∞ is typically set to unity to preserve the asymptotic behaviour of f_{ai}, N is the order of expansion, and $R_{\rm ref}$ is the expansion centre. $R_{\rm ref}$

is set to the equilibrium bond length of the lower energy electronic state. When fitting equation (19), only the B_k parameters are floated.

3.2.3 Constraining curves

The asymptotic energy limit for all the curves in Fig. 2 was constrained by setting the value of D_e^X based on the experimental value of D_0 from Joens (2001) with the added offset from the zero-point energy of the X $^2\Pi$ state, E_0^X calculated in DUO, hence

$$D_e^X = D_0 + E_0^X. \tag{20}$$

The remaining curves' D_e where constrained with respect to D_e^X such that their respective atomic limit spacings match those of Kramida et al. (2021).

3.3 Fitting – B $^2\Sigma^+$ and C $^2\Sigma^+$

These PECs were fit independently of the ground and first excited state as they are well separated from those states and their energy levels are not mutually perturbed by off-diagonal couplings of any kind. DUO calculations with the full vibrational basis in the A $^2\Sigma^+$ state from Section 3.1 were performed and compared with similar runs where the A $^2\Sigma^+$ state vibrational basis was set to have a max of $v = 1$. Comparing the energy levels of the B $^2\Sigma^+$ and C $^2\Sigma^+$ states in both cases returned the same results. The same procedure was performed to see if there is any interplay between the B $^2\Sigma^+$ and C $^2\Sigma^+$ states, and again it was confirmed that they are independent of each other, allowing for a very clean environment for fitting, where only one state needed to be considered at a time.

The need for off-diagonal couplings between the high lying $^2\Sigma^+$ states and the ground state was found empirically. A zeroth-order polynomial off-diagonal spin-orbit coupling between these states and the ground state was initialized and floated. Upon running the fitting algorithm, this value diverged, however, the energies were unchanged, indicating that spin-orbit effects here are negligible.

The PECs of these states are of a different character to those of X $^2\Pi$ and A $^2\Sigma^+$. As is visible in Fig. 2, B $^2\Sigma^+$ is very shallow relative to the other states with $D_e(B) \approx 1400\,\mathrm{cm}^{-1}$. Since the MARVEL levels available for the B $^2\Sigma^+$ state are very complete, going up to dissociation, and since the state is very shallow, the long-range shape of this potential is important. The EMO potential has seen criticism due to its inability to effectively model the long-range (Le Roy et al. 2006) and as such the MLR (Le Roy & Henderson 2007; Le Roy et al. 2009, 2011) is used here instead as given by

$$V(R) = T_e + (A_e - T_e)\left(1 - \frac{U(R)}{U(R_e)}\mathrm{e}^{-\beta(R)\xi_p(R)}\right)^2, \tag{21}$$

$$U(R) = \sum_n \frac{C_n}{R^n}, \tag{22}$$

$$\beta(R) = \xi_p(R)\beta_\infty + (1 - \xi_p(R))\sum_{i=0}^{\beta_{max}} \beta_i \xi_q(R)^i. \tag{23}$$

Here, the Morse-like parameter β is similar to that of the EMO, where it is not a constant but is implemented as a function of R, where ξ_p is the reduced coordinate from equation (13). The difference here is that order, p, is not dependent on whether the potential is calculated to the left or right of the equilibrium bond length. There is also the added parameter q allowing for the use of two separate instances of this reduced coordinate. In this study, however, $q = p$ for simplicity. β_∞ is necessarily constrained to have the following value:

$$\beta_\infty = \ln\left(\frac{2D_e}{U(R_e)}\right). \tag{24}$$

The result of this is constraint is that as $R \rightarrow \infty$, $V(R) \rightarrow U(R)$. This is the important feature of this potential. The shape set of this potential hence becomes

$$S = \{p,\ \beta_{\max},\ \{C_i\}\};\ \{p,\ \beta_{\max},\ \{i\}\} \in \mathbb{Z}. \tag{25}$$

To model the long-range of B $^2\Sigma^+$, we consider its asymptotic behaviour, where it tends to O(^{1}S) + H(^{2}S). In this limit, the primary forces between two neutral S states is Van der Waals, which has a potential form proportional to R^{-6}. Hence in the limit that $R \rightarrow \infty$, $C_n = 0$ for $n \neq 6$ (see equation 22). C_6 values for heteronuclear molecules ($C_{6,AB}$) can be calculated based on the C_6 coefficients of the individual atom pairs, $C_{6,AA}$ and $C_{6,BB}$ (Tang 1969):

$$C_{6,AB} = \frac{2C_{6,AA}C_{6,BB}}{\frac{\alpha_A}{\alpha_B}C_{6,BB} + \frac{\alpha_B}{\alpha_A}C_{6,AA}}, \tag{26}$$

where $\alpha_{A,B}$ are the polarizabilities of the individual atoms. Atomic C_6 and polarizabilities are taken from Gould & Bucko (2016). We assumed that these individual C_6 coefficients are for the ground state configurations of the atoms, which is an approximation because, in the atomic limit of B $^2\Sigma^+$, the oxygen's state is in the ^{1}S state. The $C_{6,B\ ^2\Sigma^+}$ coefficient was found using these values in conjunction with equation (26) and is given in Table 6 along with the summary of its shape set. Literature values for C_6 coefficients of excited atomic configurations do not appear to be available, and this approximation was deemed appropriate.

The vibrational structure parameter (β_i) of B $^2\Sigma^+$ was fitted to the *ab initio* curves from Section 2 and was left fixed. While fitting β_i to the MARVEL energies did somewhat improve the residuals to the said levels, this resulted in an unphysical curve which would overlap with the C $^2\Sigma^+$ state. B $^2\Sigma^+$ appears to be extremely sensitive to fitting the vibrational structure. This is likely due to most levels being close to dissociation, hence long-range effects playing a large role in the evaluation of the energy level positions. This is probably a consequence of the somewhat crude approximation made in determining C_6. Instead, a best attempt was made to fit this state by floating only T_e and R_e with the added spin-rotation constant γ, which has been used in effective Hamiltonian models for this state (Coxon et al. 1991).

C $^2\Sigma^+$ also required the use of the MLR potential. While the long-range in B $^2\Sigma^+$ is dominated by Van der Waals effects, the long-range in C $^2\Sigma^+$ is dominated by ionic interactions (Langhoff et al. 1982) as can be seen from the *ab initio* C state permanent dipole, which is linear in R at long range (see Section 6.1.2). The C $^2\Sigma^+$ state hence tends to O$^-$ + H$^+$ in the atomic limit and so for $R \rightarrow \infty$, $C_n = 0$ for $n \neq 1$. Since this is a Coulomb interaction, C_1 must be such that it is equal to unity in atomic units, $[E_h a_0]$. So all that is required to determine C_1 is a unit conversion to cm^{-1}Å resulting in the values in Table 6:

The dissociation energy of C $^2\Sigma^+$ is determined by considering the energy difference:

$$\mathrm{O}(^3\mathrm{P}) + \mathrm{H}(^1\mathrm{S}) \rightarrow \mathrm{O}^- + \mathrm{H}^+. \tag{27}$$

Hence, D_e(C) is

$$D_e(\mathrm{C}) = D_e(\mathrm{X}) + E_\mathrm{I}(\mathrm{H}) - E_\mathrm{EA}(\mathrm{O}) - T_e(\mathrm{C}), \tag{28}$$

where E_I(H) is the ionization energy of hydrogen and has been taken from Scheidegger & Merkt (2024) and E_EA(O) is the electron

Table 7. Summary of the initial parameter sets (see Section 3.2.1) for the X $^2\Pi$, A $^2\Sigma^+$, B $^2\Sigma^+$, and C $^2\Sigma^+$ states of OH.

	EMO	
Parameter	X $^2\Pi$	A $^2\Sigma^+$
T_e	0.000 000 000 000 00	32 612.251 248
R_e	0.970 655 034 637 88	1.013 454 0000
A_e	37 269.126 195 7300	53 204.256 220
p_L	4	3
p_L	3	3
N_L	6	4
N_R	8	8
β_0	2.292 052 187 440 86	2.620 3960
β_1	−0.019 995 180 618 05	0.169 7680
β_2	0.198 099 685 501 73	0.465 2890
β_3	0.231 459 916 196 33	0.552 2080
β_4	−0.136 025 0120 3037	0.413 9210
β_5	−0.639 517 770 410 11	−5.174 652
β_6	−0.277 770 705 585 67	9.999 9980
β_7	6.274 892 232 438 52	3.333 8650
β_8	−4.898 195 1459 0987	−9.999 764
	MLR	
Parameter	B $^2\Sigma^+$	C $^2\Sigma^+$
T_e	70 048.640 000	89 072.338 876[a]
R_e	1.862 703 0000	2.03204[a]
A_e	71 294.380 000	135 395.846 9789
p	2	2
β_0	−0.656 9361	1
β_1	6.320 934	0
β_2	10	0
β_3	6.522 668	0
C_1	0	11 6140.926 2795[b]
C_6	47 686.64[b]	0

[a] Not pre-fitted, but simply taken from *ab initio* values.
[b] Calculated see Section 3.3.

affinity of oxygen and has been taken from Kristiansson et al. (2022). D_e(C) and C_1 have been left fixed during the fitting procedure and the pre-fitting procedure was forsaken here in favour of doing this empirically. This was done due to the *ab initio* curves being incomplete at short R. The *ab initio* calculation provides a starting value for T_e. The PEC parameters left floating here are β_0, T_e, and R_e, with $p = 2$. As with B $^2\Sigma^+$, a spin-rotation constant was added as this had been used in the available effective Hamiltonian treatments (Coxon et al. 1991). Summarizing, the shape set is given in Table 6. These were initially paired with the parameter sets in Table 7.

Along with the refinement of the PECs and coupling curves as described above, empirical coupling constants were also implemented with more details available in Section 6.1. When satisfactory agreement was reached with the reference energy levels, the final line list is calculated using DUO, producing the .STATES and .TRANS files. Initially, these files contain all states and transitions, including bound states and continuum states, the latter of which are treated in a separate process, leading to continuum absorption (.CONT) files (see Section 5.2). The methods implemented to isolate bound states is explained in the following section.

4 METHODS: BOUND AND UNBOUND ROVIBRONIC STATES

Rovibronic states calculated with DUO are constrained by the boundary condition that the wavefunction, ψ is zero at the end of the calculation box, R_c, where the potential $V = \infty$. In this regime, all states are effectively treated as bound states, with a node at R_c. To treat continuum states rigorously using DUO, one must have R_c at ∞ which is not possible. In this section, the categorization of bound versus unbound states in DUO is discussed. The details of how unbound states and quasi-bound states are treated in the context of spectral simulation of continuum absorption is discussed in Section 5.

An important clarification at this stage is that the rovibronic levels and their corresponding wavefunctions which are considered in this section are calculated from a spectroscopic model containing only X $^2\Pi$ and (A, B, C) $^2\Sigma^+$. In this treatment, the quasi-bound character induced by spin-orbit predissociation effects in A $^2\Sigma^+$ do not manifest as the relevant continuum states and couplings are not included in this model. Continuum rovibronic states where the term value $> D_e$ of the respective electronic state continue to be present, however.

The assumptions here are that (1) in the full treatment (predissociation included), if a quasi-bound state in A $^2\Sigma^+$ with quantum numbers, $\mathbf{Q}$ exists, then the corresponding state in this four-state model with the same $\mathbf{Q}$ is bound and (2) all states in the four-state model with $\mathbf{Q}$ which are unbound remain unbound in the full treatment. In reality, only levels in X $^2\Pi$ and A $^2\Sigma^+$ which are energetically lower than the dissociation limit of X $^2\Pi$ are truly bound due to predissociation effects. All other, higher energy states are either continuum states or quasi-bound states. The aim of this section is to find states which should be included in the line list, which has the criterion that continuum states are not included, but quasi-bound states are included. With this assumption in place, states referred to as bound hereafter are necessarily bound only in this four-state treatment, but may be quasi-bound in the full treatment.

The purpose of doing this analysis is twofold. First, it constrains the levels which are included in the final line list. Secondly it constrains the range of states in A $^2\Sigma^+$ which require predissociation lifetime calculation by requiring that such states are bound in this four-state model and also have energy greater than the dissociation limit of X $^2\Pi$. Further discussion of predissociation is available in Section 5.1.

4.1 Differentiating between bound and unbound states

As stated above, the boundary condition on ψ results in all states effectively being treated as bound states. There is, however, a unique character to the wavefunction of bound states and continuum states even in the strictly bound regime in which DUO calculations are performed. Due to the presence of an effective infinite potential at the boundary, R_c, bound state wavefunction solutions tunnel through the right-hand side of the potential well to reach zero and exhibit an exponential decay form in this region. On the other hand, for continuum states, as there is no potential barrier through which to tunnel, they exhibit a sinusoidal wave form. This difference is showcased in Fig. 5.

As the characteristic of a bound state is a decaying wavefunction with close to zero amplitude at R_c, in the region between $R_c - \epsilon$ and R_c, where ϵ is some small length, the integral, $\int_{R_c-\epsilon}^{R_c} \left|\psi^2(R)\right| \, \mathrm{d}R$ is also close to zero. For unbound states, this integral is not close to zero.

In the rigorous case, where $R_c \to \infty$:

$$\int_{R_c-\epsilon}^{R_c} |\psi(R)|^2 \, \mathrm{d}R = \begin{cases} 0 & \text{for bound states} \\ > 0 & \text{for unbound states} \end{cases}. \tag{29}$$

Numerically, this problem is not so clear cut and one must establish a threshold value above which states are labelled as unbound. The value of the integral is also dependent on ϵ and as such the threshold

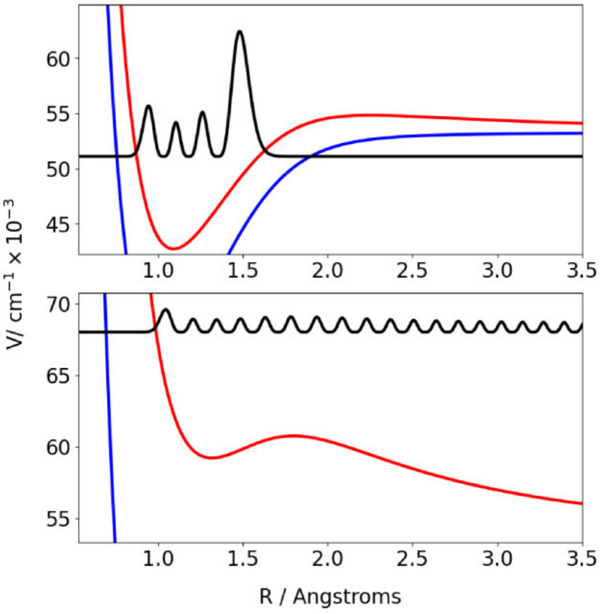

Figure 5. Example of bound state (upper panel) and unbound state (lower panel) wavefunction radial densities for the A $^2\Sigma^+$ state of OH. The red line is the effective potential $V_{\rm eff}(R)$ (see equation 31), and the blue line is the unperturbed potential $V(R)$. Baseline of the wavefunction has been placed to sit at level's energy, and the amplitude has been scaled for clarity only.

is dependent on the value of ϵ taken. Loosely, one can think of δ_I as a function of ϵ where the function returns a 'useful' value for the threshold. Hence, we have the threshold, $\delta_I(\epsilon)$ and equation (29) becomes

$$\int_{R_{\rm c}-\epsilon}^{R_{\rm c}} |\psi(R)|^2 \; {\rm d}R = \begin{cases} \le \delta_I(\epsilon) & \text{for bound states} \\ > \delta_I(\epsilon) & \text{for unbound states.} \end{cases} \tag{30}$$

In studying the wavefunctions of OH, a value of ϵ is taken at 0.5 Å which is default in DUO. One may use other values. As default, the value of δ_I in DUO is set to $\sim 10^{-8}$. Note, that this value is somewhat arbitrary and there does not appear to be an intuitive value one can take for δ_I. The question now is how can a reasonable value of δ_I be determined?

Before continuing further, one can suggest another method to categorize bound versus unbound states. The PEC, $V(R)$ becomes distorted at high rotational quanta, as the molecule becomes stretched. Hence, the effective equilibrium bond length for a given J increases. To account for this, one can use the effective potential form (Kozin, Roberts & Tennyson 1999),

$$V_{\rm eff}(R) = V(R) + B(R)J(J+1), \tag{31}$$

where $B(R) = \frac{h}{8\pi^2 c\mu R^2}$ in cm^{-1}, c is the speed of light, μ is the reduced mass of the molecule, and h is Planck's constant. This rotational term increases the effective dissociation energy (here defined as the potential maximum to the right side of $R_{\rm e}$), of the molecule, $\tilde{D}_{\rm e}(J)\big(\tilde{D}_{\rm e}(0) = D_{\rm e}\big)$, and in cases where the reduced mass is low, such as in OH, this effect can be significant. In Fig. 6, we see how as J increases, so does $\tilde{D}_{\rm e}(J)$. Indeed, $T_{\rm e}(J)$ is also increasing and the resulting effective PEC becomes shallower. The position of the minimum, $R_{\rm e}$ is also shifted by the rotational perturbation and becomes a function of J. For higher J at long range, $\tilde{D}_{\rm e}(J)$ is no longer asymptotic and instead occurs at a turning point at some $R = \tilde{R}(J)$, causing a barrier through which the wavefunction can tunnel. This tunnelling broadens the energy level, causing rotational predissociation (Yurchenko et al. 2024).

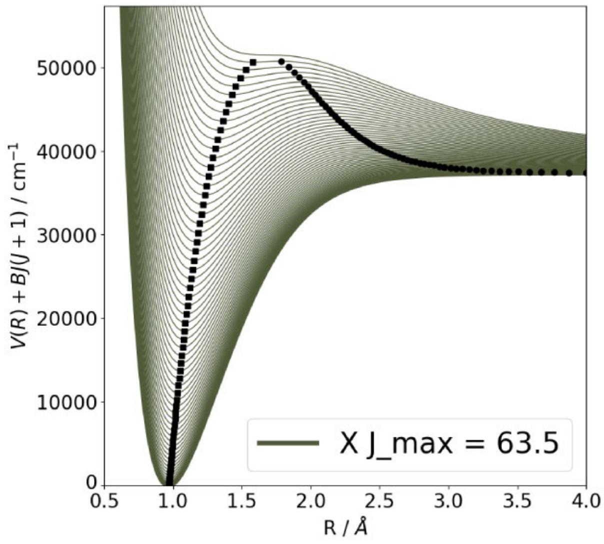

Figure 6. Effective PECs of OH X $^2\Pi$ state for every J up to 63.5. The dotted curves indicates $\tilde{D}_{\rm e}(J)$ at $\tilde{R}(J)$ and the curve of squares indicates $T_{\rm e}(J)$ at $R_{\rm e}(J)$.

To this end, one can approximately assume that a state is bound for a given J if its energy falls between $T_{\rm e}(J)$ and $\tilde{D}_{\rm e}(J)$. While this makes some intuitive sense, this is a cruder approximation than the rigorous analysis of the wavefunctions. It is, however, useful to compare this crude model to the results from the wavefunction in terms of efficacy in categorizing different state types.

We arrive at an appropriate value of δ_I, in part, by comparing these two models. We define two categories here, Type C, and Type W bound/unbound, corresponding to the effective, *centrifugal* potential approximation and *wavefunction* treatment, respectively.

An energy level is Type C bound if its term value lies between $T_{\rm e}(J)$ and $\tilde{D}_{\rm e}(J)$ and is Type W bound if $\int_{R_{\rm c}-\epsilon}^{R_{\rm c}} \left|\psi^2(R)\right| \; {\rm d}R < \delta_I$.

We also define three types of potential energy: *Unperturbed*$(V(R))$, *perturbed*$(V_{\rm eff}(R;J)$, with a finite $\tilde{D}_{\rm e}(J)\big)$, and *repulsive* (no minima/maxima). An example of a repulsive type is shown in Fig. 6 for $V_{\rm eff}$ at $J \geq 63.5$.

We require that all states which are known to be bound experimentally, must be bound in the wavefunction treatment. In this case, this is found by calculating $\int_{R_{\rm c}-\epsilon}^{R_{\rm c}} \left|\psi^2(R)\right| \; {\rm d}R$ for all states using the spectroscopic model from Section 3 and isolating the states which appear in the MARVEL data set. This data set is quite complete and goes up in energy up to $D_{\rm e}$ for the X $^2\Pi$, A $^2\Sigma^+$, and B $^2\Sigma^+$ states. Hence, this is a good measurement for reasonable bound integral values. For simplicity, here we examine the X $^2\Pi$ and A $^2\Sigma^+$ states only.

Fig. 7 plots the values of the integral $\int_{R_{\rm c}-\epsilon}^{R_{\rm c}} \left|\psi^2(R)\right| \; {\rm d}R$ as a function of J for all MARVEL levels of the X $^2\Pi$ and A $^2\Sigma^+$ states of OH. It shows that the majority of experimentally determined (MARVEL) states have integrals below 10^{-8}. This supports the original value of the threshold integral. However, this threshold does not extend well to energies above $D_{\rm e}$ but below $\tilde{D}_{\rm e}(J)$, which are quasi-bound due to rotational predissociation effects.

Extending the plot to higher energies, we notice that at some J there is a discontinuity in the integral where it suddenly rises, indicating that the region is transitioning from bound to unbound. We find evidence that this is the case for $v = 0$ of the A $^2\Sigma^+$ state.

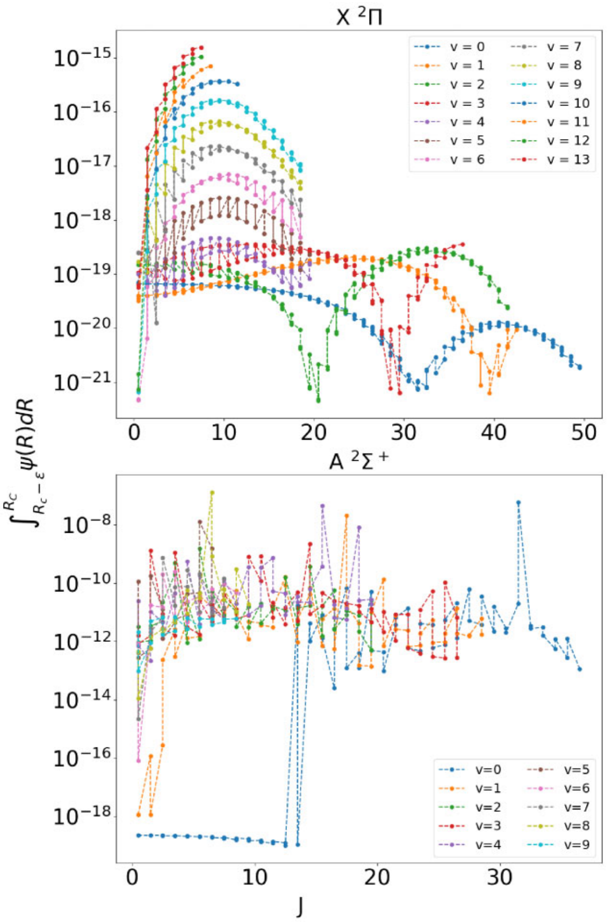

Figure 7. $\int_{R_c-\epsilon}^{R_c}\left|\psi^2(R)\right|\,\mathrm{d}R$ for each MARVEL level of the X $^2\Pi$ and A $^2\Sigma^+$ states of OH.

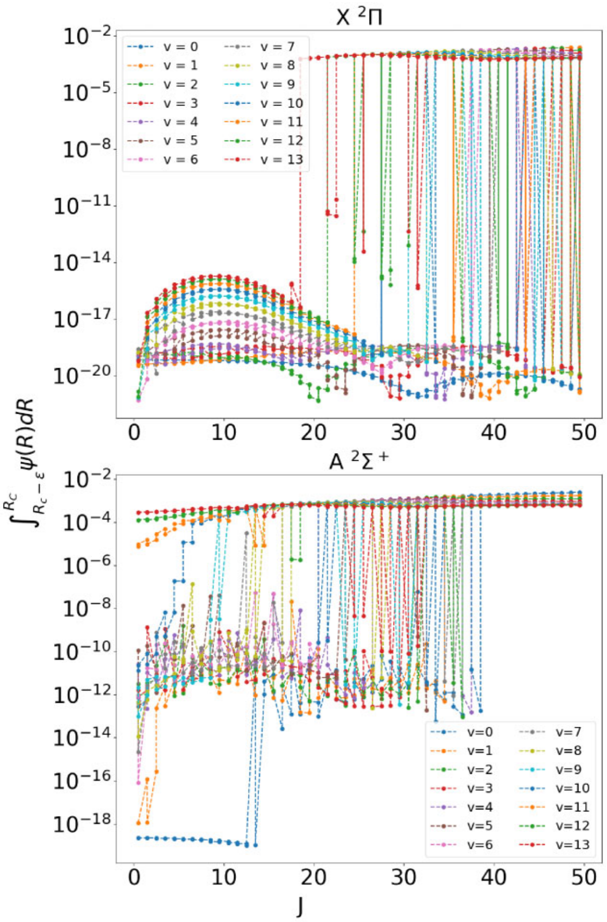

Figure 8. $\int_{R_c-\epsilon}^{R_c}\left|\psi^2(R)\right|\,\mathrm{d}R$ for each v, J of the X $^2\Pi$ and A $^2\Sigma^+$ states of OH.

This vibrational level contains the most MARVEL levels and goes up to $J = 36.5$. At this J, the integral is of the order of 10^{-13}. When considering all levels that are calculable, at $J = 37.5$ the integral increases suddenly to 10^{-3}. A similar discontinuity occurs at $v = 1$.

The approach in identifying continuum states is to look for discontinuities in the J-dependence of $\int_{R_c-\epsilon}^{R_c}\left|\psi^2(R)\right|\,\mathrm{d}R$. Fig. 8 shows that the majority of states pre-discontinuity appear with integrals $< 10^{-6}$. This threshold allows for the inclusion of many borderline states, but does not include states which lie at $v = 10+$ for the A $^2\Sigma^+$ state, which have not been detected experimentally. The X $^2\Pi$ state is clearer in that the integral quite consistently increases from 10^{-20} to 10^{-3}.

It is clear that this method for determining the appropriate threshold δ_I for the bound/unbound selection is rather approximate. When producing a line list, the aim is to have only bound and quasi-bound states present in the .STATES and .TRANS file. When considering the A $^2\Sigma^+$ state, where the line between bound and unbound in the wavefunction treatment is not well defined, this is difficult to do. The decision was made that it is better to include too many states in the line list rather than too few, especially since states which are unbound are expected to have very low intensity so should not affect the spectrum simulation significantly. Such states are not excluded, however, and are instead treated as continuum absorption transitions in Section 5.2.

With this threshold established, all energy levels from the calculation have been assigned Type W bound or unbound tags for the threshold value of $\delta_I = 10^{-6}$. Comparing the Type W and Type C tags shows that many states in the effective potential approximation which would be assigned as bound have been assigned as Type W unbound, see Table 8.

Table 8. Tabulated comparison between Type C and Type W categorizations of bound versus unbound states. Type C unbound states are states for which $T_\mathrm{e}(J)$, $\tilde{D}_\mathrm{e}(J)$ are finite but $E > \tilde{D}_\mathrm{e}(J)$, this is distinct from repulsive, where in the effective potential approximation, all states are unbound as $T_\mathrm{e}(J)$, $\tilde{D}_\mathrm{e}(J)$ are undefined. Dark states are states where $E < T_\mathrm{e}(J)$ and are present likely due to misassignments in the manifold. Calculated with $\epsilon = 0.5$ Å and $\delta_I = 10^{-6}$. N is the count.

Manifold	Type C	N(Type W unbound)	N(Type W bound)
X $^2\Pi$	Bound	2300	2250
	Unbound	17195	0
A $^2\Sigma^+$	Bound	968	547
	Dark	559	0
	Unbound	13 268	0
	Repulsive	300	0
B $^2\Sigma^+$	Bound	156	59
	Dark	121	0
	Unbound	6383	3
	Repulsive	6443	0

We see that approximately two-thirds of A $^2\Sigma^+$ Type C bound states have been assigned Type W unbound status and similarly, this

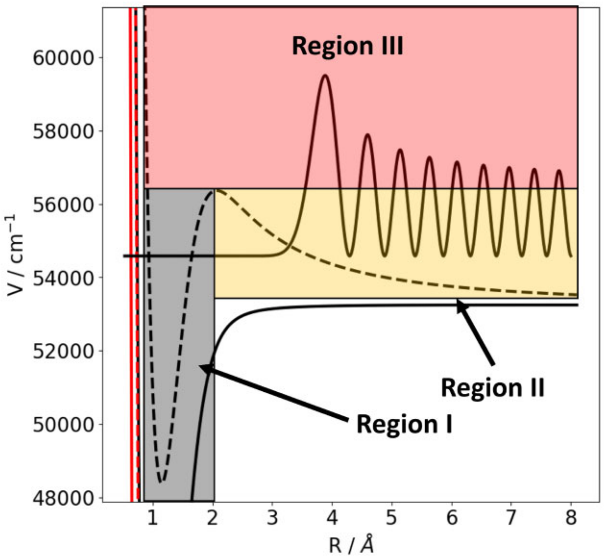

Figure 9. Toy example of computed wavefunction probabilty distribution where Type C is bound but Type W is unbound. Solid lines represent unperturbed PECs and dashed lines represent the effective A $^2\Sigma^+$ state PEC. The probability has been scaled for visibility and shifted so that zero probability lies at the correct energy. Region I: $R_{\rm min} < R < \tilde{R}(J)$ and $E < \tilde{D}_{\rm e}(J)$, Region II: $R > \tilde{R}(J)$, and Region III: $E > \tilde{D}_{\rm e}(J)$.

happens to half of the X $^2\Pi$ states. Fig. 9 shows an example of one such state in the A $^2\Sigma^+$ state. It is clear that this is state is unbound as the wavefunction density is entirely located to the right of the rotational barrier. This shows a limitation in considering only the energy in the categorization of quasi-bound and unbound rovibronic levels, as this level's energy lies between $T_{\rm e}(J)$ and $\tilde{D}_{\rm e}(J)$.

Focusing specifically on the X $^2\Pi$ and A $^2\Sigma^+$ states for simplicity, the average integral for these oppositely categorized states is $\sim 6.7 \times 10^{-4}$. Increasing the threshold to this average value is unfavourable as this allows for the majority of Type C unbound states to be categorized as Type W bound.

This also further highlights the inefficacy of the effective potential approximation as it has been applied here. Considering only the energy value of a given level ignores the details of what is now, effectively, a scattering problem.

At this point, it is important to note that all but 12 of the 3154 energies with this opposite categorization in Table 8 are for cases where the energy of the level is greater than the *unperturbed* dissociation energy of the relevant PEC and none of these states have been observed experimentally as is corroborated in the discussion of Fig. 7 earlier.

To conclude the analysis of this problem, it is necessary to consider the impact of these borderline Type C bound, Type W unbound states on the intensity. Intensity calculations are performed for $T = [300, 2000, 5000]$ K for all transitions where the final state types are

(i) Subset 1 – $^1\sigma$: Type C bound + Type W unbound.
(ii) Subset 2 – $^2\sigma$: Type C bound + Type W bound.

The integrated intensities for transitions between states in $^1\sigma$ and transitions between states in $^2\sigma$ are calculated and compared as a measure of this impact. Intensities are calculated using the standard formula:

$$I(f \leftarrow i) = \frac{g_f^{\rm tot} A_{fi}}{8\pi c \nu_{fi}^2} \frac{{\rm e}^{-c_2 E_i/T}\left(1 - {\rm e}^{-c_2 \nu_{fi}/T}\right)}{Q(T)}, \tag{32}$$

where the partition function $Q(T)$ is defined as

$$Q(T) = \sum_n g_n^{\rm tot} {\rm e}^{-c_2 E_n/T}. \tag{33}$$

Here, $g_n^{\rm tot} = g_n^{ns}(2J_n + 1)$ is the total degeneracy for the nuclear-spin statistic g_n^{ns}, $c_2 = 1/k_{\rm b}$ is the second radiation constant in cm K and T is the temperature in K.

The intensities for the $^1\sigma$ and $^2\sigma$ subsets are summed and compared. It was found that the intensity of $^2\sigma$ is significantly dominant, especially at lower temperatures, even considering that the majority of rovibronic states are not included in this calculation. At 5000 K, less that 1 per cent of the integrated intensity is accounted for by states in $^1\sigma$. In light of this analysis, the threshold value has been chosen such that $\delta_I = 10^{-6}$ as this has been found to exclude all high-energy unbound states while preserving intensity to highest reasonable amount. Reiterating, these lines are not excluded in the simulation of the absorption cross-section, and are instead shifted to be part of the continuum analysis (Section 5.2), meaning that none of this intensity, however, small, will be neglected in the data given in the supplementary material.

4.2 Uncertainty in vibrational assignment

Fig. 9 separates the PEC into three distinct regions. Region I covers the potential well, Region II covers the space between the right side of the well and $R_{\rm c}$, and Region III covers the space above $\tilde{D}_{\rm e}(J)$. As was stated above, the effective potential categorization is not a sufficient metric for determining if a state is bound or unbound due to the presence of states in Region II.

This introduces another element of uncertainty when considering the quantum number labelling. In the DUO solution method, J and τ are the only rigorous labels applied along with an enumerator n, counting up in energy. The rest are best estimates based on energy ordering and/or basis set contributions. The scheme in which the calculations for OH are performed is such that the vibrational quanta are counted in order of energy within the J, τ symmetry block. This is already not a perfect solution, but becomes even more problematic when considering the presence of states in Region II.

Vibrational quanta are counted, assigned to an electronic state, and then normalized to start at 0 for the given electronic state. One can visualize the PEC in Region II, effectively as an induced repulsive PEC, A^* $^2\Sigma^+$. During the calculation, it is not easy to differentiate whether a state belongs to A $^2\Sigma^+$ or A^* $^2\Sigma^+$. These repulsive states then have a meaningful effect on the vibrational labelling of the bound states, which results in bound states with anomalously high vibrational quanta labelled as bound. This is not a problem when simulating the spectrum, as these quantum numbers are not considered, only the rigorous quantum numbers from before along with their enumerator, n. This does mean, however, that when producing the line list, that the quantum labels must be considered unreliable for all levels with energy above $D_{\rm e}$ for their respective electronic state.

At this stage, the line list has been effectively separated into subsets containing bound–bound/quasi-bound transitions (.STATES and .TRANS files) and bound–unbound transitions (.CONT files). In line with ExoMol standards for .STATES files, the radiative lifetimes are calculated at this stage and are convoluted with available predissociation lifetimes to produce the lifetimes column. Landé g-factors are calculated, and estimates for uncertainties are produced in line with the predicted shifts (PSs) method.

4.3 Predicted shifts method

Interpolated observed – calculated corrections are fit based on the known observed – calculated energy shifts seen in other levels with the same spin-orbit, parity and vibronic assignments (Bowesman et al. 2024). This procedures avoids discontinuities between MARVEL energy levels and those calculated with Duo (McKemmish et al. 2024). The spin-orbit, parity and vibronic assignments are used to divide the data into different groups, such that independent fits can be performed over each subset. This means perturbations that may appear in one subset can be treated independently, without impacting the quality of the fits to other data. Within these subsets of levels, the observed – calculated energy differences are fit as a numerical function of the principal quantum number, which was taken as J here. Once a fit to the known data has been performed, predictions can be made for any levels not contained within the MARVEL data set based on their corresponding values of J. Similarly, uncertainties can be determined for levels corrected with these predicted energy shifts, based on the uncertainties in the MARVEL energies that were fit to, and based on the mean standard error of the fit. For a level with an energy set with PSs, $\tilde{E}_{\rm PS}$, obtained from a fit to n observed – calculated data points, the uncertainty in this energy is obtained as

$$\Delta\tilde{E}_{\rm PS} = \sum_{i=1}^{n} \frac{\Delta\tilde{E}_i + |\delta_i - \delta_i^{\rm pred}|}{n}, \tag{34}$$

where δ_i a the observed – calculated value of the ith level fit to and $\delta_i^{\rm pred}$ is the corresponding observed – calculated value obtained in the fit.

5 METHODS: SIMULATION OF ABSORPTION SPECTRA

We follow the convention (Tennyson et al. 2023) of including all bound–bound and bound–quasi-bound transitions (see Section 4) in the standard ExoMol .STATES and .TRANS files (Tennyson, Hill & Yurchenko 2013), while bound–unbound transitions are compiled in separate .CONT (continuum absorption) files. This file was produced using PYEXOCROSS for $T \in [100, 200, ..., 8000]$ K with a grid spacing of 0.01 cm^{-1} with the procedure covered in 5.2.

5.1 Predissociation lifetimes

Predissociation lifetimes for the A $^2\Sigma^+$ state of OH were made available in the supplementary material of Paper I. As mentioned before, these lifetimes are not based on the updated spectroscopic model presented here and so are recalculated using the same method. The work in Section 4 constrained analysis of predissociation in A $^2\Sigma^+$ to 547 rovibronic levels, returning 414 non-trivial predissociation lifetimes.

Total lifetimes are included in the .STATES file in a dedicated lifetime column (Tennyson et al. 2023). As standard, this column is populated with the radiative lifetime, which is related to the reduced sum of Einstein-A coefficients that pertain to that state:

$$\tau_{\rm rad}(f) = \sum_{i<f} \frac{1}{A_{fi}}, \tag{35}$$

where $\tau_{\rm rad}$ is the radiative lifetime of the upper state f and A_{fi} are its Einstein-A coefficients. To include the predissociation lifetime of the A $^2\Sigma^+$ state, $\tau_{\rm prediss}$, we consider that the lifetime of the upper state in a transition determines the lifetime broadening parameter, Γ, the full width at half-maximum,

$$\Gamma(f) = \frac{1}{2\pi c\tau(f)}, \tag{36}$$

where the f denotes that this is the lifetime of the upper state in the transition, τ is the lifetime in s, and c is the speed of light in cm s^{-1}. To account for the two sources of lifetime broadening, one sums their individual broadening parameters,

$$\Gamma_{\rm tot} = \Gamma_{\rm rad} + \Gamma_{\rm prediss}. \tag{37}$$

Hence, as per equation (36), we arrive at the total lifetime,

$$\tau_{\rm tot} = \frac{\tau_{\rm rad} + \tau_{\rm prediss}}{\tau_{\rm rad}\tau_{\rm prediss}} \tag{38}$$

which, for the A $^2\Sigma^+$ state is reported instead of the radiative lifetime. The B $^2\Sigma^+$ state is also known to predissociate due to crossings with the local 2 $^2\Pi$ state (van Dishoeck & Dalgarno 1984a, 1984b; Sun et al. 2020). Hwang et al. (2001) experimentally found that the total lifetimes of the $v = 0$ band of B $^2\Sigma^+$ are of the order of 100 ns for $J = 0.5$ decreasing exponentially to 10 ns for $J = 4.5$, which they claim agree well with Sappey, Crosley & Copeland (1989). These data are not available however, and are only given as plots, so making use of them is difficult. Furthermore, the 2 $^2\Pi$ state and its coupling to the B $^2\Sigma^+$ state has not been considered in this study so calculating these lifetimes is not possible. Similarly, due to the high-lying nature of the C $^2\Sigma^+$ state and the presence of many Rydberg states in this region, some of which may be repulsive, it is expected that this state would be predissociative. The computations required to assess this are, however, prohibitively expensive. Lastly, transitions in the region of the B $^2\Sigma^+$ and C $^2\Sigma^+$ bands are dominated by continuum absorption, meaning that these effects are likely unimportant, as total integrated intensity does not change upon the inclusion of predissociation, only the distribution of intensity. These predissociative effects have not been considered in this study and the radiative lifetimes for B $^2\Sigma^+$ and C $^2\Sigma^+$ are reported instead, with further study into the predissociation of OH left as future work.

5.2 Continuum absorption spectra

Along with the .STATES and .TRANS files, the convention of including continuum absorption spectra in separate .CONT files began with the AlHambra line list for AlH (Yurchenko et al. 2024) and is replicated here. Direct continuum transitions going from X $\rightarrow$ R where R $\in$ [1 $^2\Sigma^-$, 1 $^2\Delta$, A $^2\Sigma^+$, B $^2\Sigma^+$] is a repulsive electronic state are computed. Note that for A$^2\Sigma^+ \leftarrow$ X$^2\Pi$ and B $^2\Sigma^+ \leftarrow$ X$^2\Pi$, only states which are Type W unbound (see Section 4) are considered in this calculation.

As discussed before, in the DUO treatment, all states – continuum or not – are treated as bound states. Due to the bound-like boundary conditions imposed in this solution of the Schrödinger equation, the continuum spectrum is effectively discretized, and requires further post-processing to return physical results. An example from OH is given in Fig. 10, where the continuum absorption spectra are produced using EXOCROSS at 300 K with a Gaussian HWHM, $\alpha = 10$ cm^{-1} which showcases this discrete nature. This is unphysical as continuum absorption spectra are expected to be continuous due to the infinite density of states of repulsive PECs. Pezzella, Yurchenko & Tennyson (2021) developed a method to deal with this through the use of Gaussian smoothing and this has been applied to HCl and HF by Pezzella, Yurchenko & Tennyson (2022) giving good agreement with continuous cross-sections from literature. Here, this method is modified somewhat for application to OH to produce

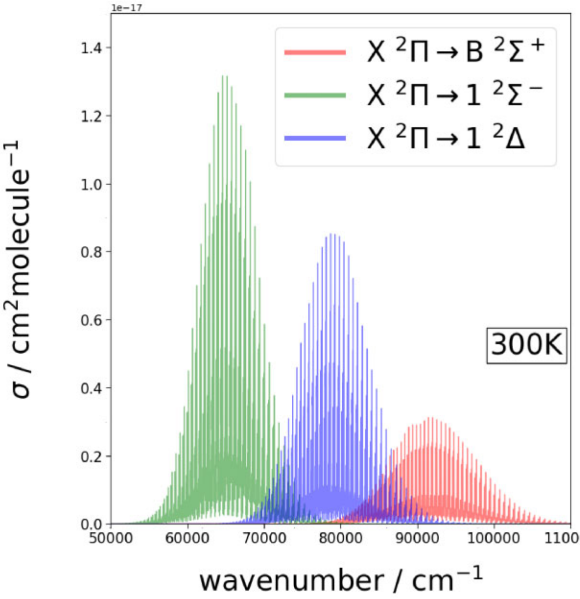

Figure 10. Initial continuum absorption cross-sections calculated for OH using ExoCross with $\alpha = 10\,\mathrm{cm}^{-1}$.

optimally smoothed continuum absorption cross-sections (Pezzella et al. 2024); full details of this methodology are the subject of a forthcoming paper (Mitev et al., in preparation).

6 RESULTS

6.1 Spectroscopic model of OH

The resulting *ab initio* PECs and coupling curves obtained for the X $^2\Pi$ and A,B,C ($^2\Sigma^+$) electronic states were fit against empirically derived Marvel energy levels from Furtenbacher et al. (2022) as per the methodology described in Section 3. The fitted model reproduces experimental data with a root mean square error (RMS) of the order of 2.7 cm^{-1}. While this is significantly higher than typical ExoMol line lists, this figure is skewed by residuals in the B $^2\Sigma^+$ state, which could not be adequately fit due to difficulties in modelling the long-range and its energy levels' anomalously high sensitivity to the shape of the potential. Furthermore, fitting in the C $^2\Sigma^+$ state is halted at a higher RMS than is typical as energy levels here have uncertainties on average at $\sim 0.5\,\mathrm{cm}^{-1}$; fitting to higher resolution would likely result in an overfitted model. Finally, the A $^2\Sigma^+$ state is strongly perturbed by the local continuum states 1 ($^2\Sigma^-$,$^4\Sigma^-$,$^4\Pi$) (Paper I; Kozlov et al. 2024), whose effects could not be fully included, which reroutes off-diagonal rotational structure considerations entirely to the $\langle \mathrm{X}|\hat{H}_{\mathrm{SO}}|\mathrm{A}\rangle$ term. These challenges are circumvented through the use of hybridization and the PSs methodology, which is made more robust by the completeness of the Marvel energies in X $^2\Pi$ and A $^2\Sigma^+$. Average RMS values are given for each v, State in Table 9.

6.1.1 Potential energy and coupling curves

The curves which compose the spectroscopic model of OH were refined to reproduce the empirical Marvel data set by Furtenbacher et al. (2022) by floating the parameters R_e(X,A,B,C), T_e(X,A,B,C), β_i(X,A,C) (PECs), and B_k (spin-orbit and L-uncoupling curves).

Table 9. RMS errors for each v, State in the MYTHOS model energies as compared to empirical energy levels from Marvel data set by Furtenbacher et al. (2022). Total RMS = 2.673 70 cm^{-1}.

	RMS(v)			
v	X $^2\Pi$	A $^2\Sigma^+$	B $^2\Sigma^+$	C $^2\Sigma^+$
0	0.258 37	0.136 91	19.475 53	0.423 61
1	0.152 37	0.168 64	12.130 49	0.522 67
2	0.214 68	1.066 52		
3	0.121 11	0.832 90		
4	0.103 89	0.656 88		
5	0.071 03	1.865 16		
6	0.096 88	2.874 05		
7	0.143 97	4.362 75		
8	0.153 29	1.997 29		
9	0.287 88	4.332 98		
10	0.308 26			
11	0.526 50			
12	0.931 93			
13	0.839 94			
Total	0.274 62	1.688 78	16.596 41	0.475 72

Couplings to other electronic states have not been considered here for sake of simplicity in the model. Furthermore, couplings to the repulsive electronic states, 1 ($^2\Sigma^-$,$^2\Delta$,$^4\Sigma^-$,$^4\Pi$), have not been considered either. To have included these couplings would have made the fitting calculations prohibitively expensive and the resulting spectroscopic model dependent on the box size selected in Duo (Mitev 2024; Mitev et al., in preparation).

Along with the adjusted PECs and the *morphed* coupling curves, two more empirical, diagonal constants have been introduced to account for the aforementioned missing considerations (Tennyson et al. 2016). These are the spin-rotation, γ(X,A,B,C), and the Λ-doubling, α_{p2q}(X) and q(X) (Brown, Cheung & Merer 1987). The inclusion of such factors was necessary to refine the energy level reproduction without the introduction of further electronic states or off-diagonal couplings. These factors have been seen in effective Hamiltonian treatments of these states (Coxon et al. 1991; Brooke et al. 2016; Yousefi et al. 2018)

A polynomial function $C(R)$ has been used as the parametric representation for these empirical factors,

$$C(R) = \sum_{i=0} A_i (R - R_\mathrm{e})^i, \tag{39}$$

where A_i is the polynomial expansion coefficient. For all factors, $A_i = 0$ for $i \geq 1$, except for γ(B), where A_1 has also been fitted due to the complex rotational structure. In Duo, one can fit the spectroscopic model both against data sets of energy levels and of transitions. The process taken in this work was to fit against the experimentally derived Marvel energy levels by Furtenbacher et al. (2022). The fitted parameters for PECs, SOCs, EAMCs, and empirical coupling constants are made available in the supplementary input files, see Section 7.

Visualizations of the final PECs and morphed coupling curves are given in Figs 2, 11, and 12.

6.1.2 Transition and permanent dipole moment curves

The *ab initio* permanent and transition dipole moments for the OH molecule are presented in Figs 13 and 14, respectively. The transition dipole moments are in good agreement with the available literature values from van der Loo & Groenenboom (2005), Yousefi et al. (2018), Langhoff et al. (1982), van Dishoeck et al. (1983), Brooke et al. (2016), Yarkony (1992), and a comparison is given in Fig. 15.

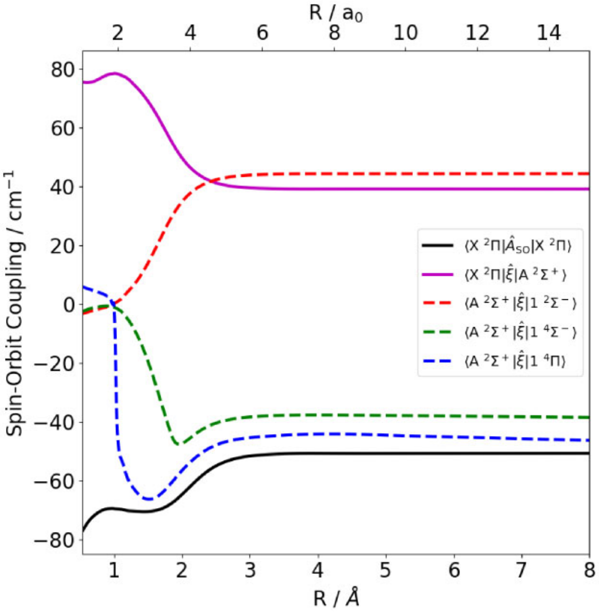

Figure 11. Spin-orbit couplings are used in the spectroscopic model of OH. Solid lines: bound–bound line list, dashed lines: predissociative broadening only.

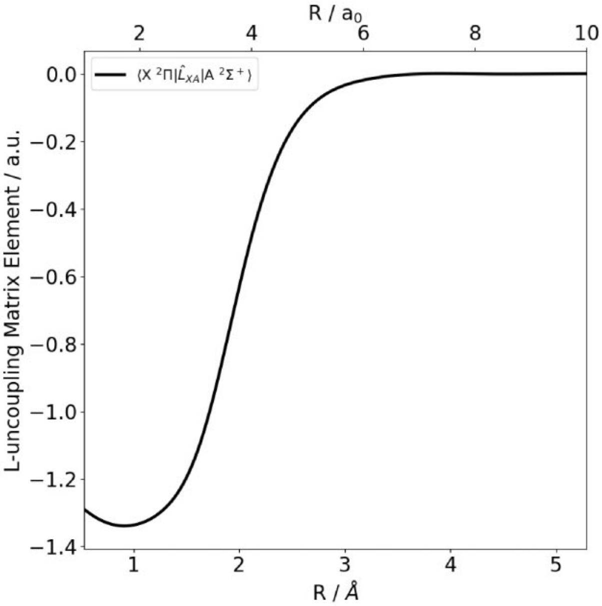

Figure 12. L-uncoupling curve used in spectroscopic model of OH.

The C $^2\Sigma^+$ is ionic at long range as is confirmed by its permanent dipole moment from Fig. 13 which, at long range, scales linearly with R.

The dipoles presented in these figures are *ab initio* and are used as such in the DUO input file for the calculation of Einstein-A coefficients. In the nuclear motion calculation, the ground state permanent dipole was originally represented in the form of 28 grid points between ∼ 0.53 and ∼ 5.3 Å. The DUO defined grid is significantly more dense, with 1001 points between 0.53 and 8 Å. Values between the input grid points are found by interpolation using cubic splines in DUO. X–X transition intensities are expected to be negatively correlated with vibrational excitations and that there is some proportionality such that,

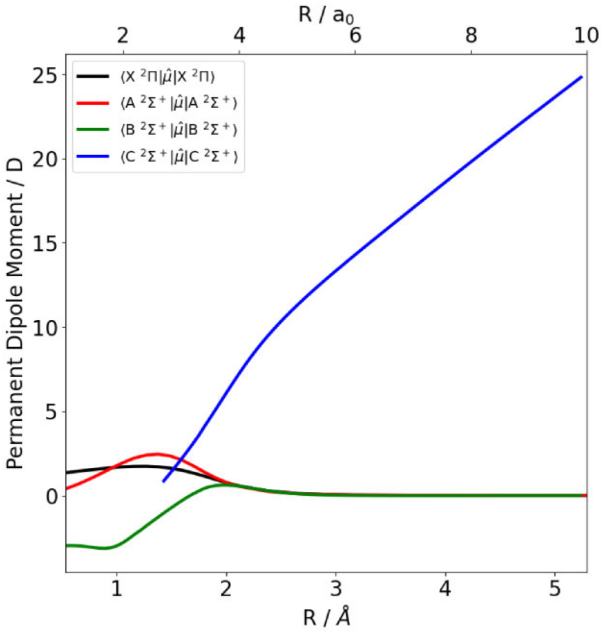

Figure 13. Permanent dipole moment curves used in spectroscopic model of OH. These are *ab initio*, and are taken directly from MOLPRO.

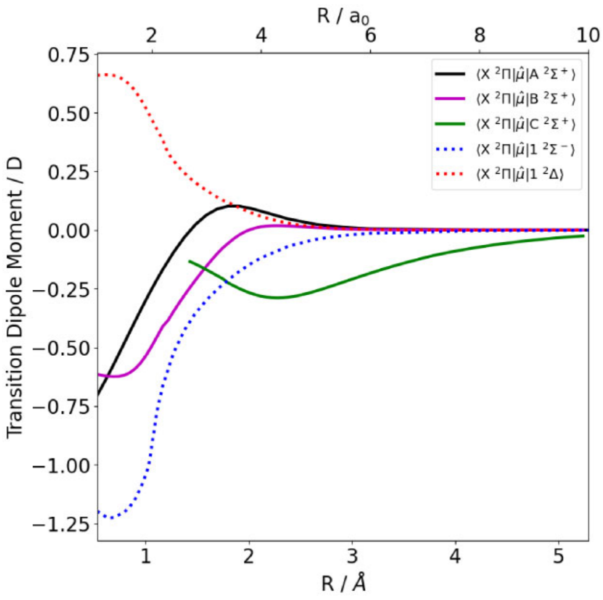

Figure 14. Transition dipole moment curves used in spectroscopic model of OH. These are *ab initio*, and are taken directly from MOLPRO, x-component only. Solid lines: bound–bound line list, dotted lines: continuum absorption only.

$$\log_{10} I(\Delta_v) = -K_v \Delta_v, \tag{40}$$

where $\Delta_v = v_f - v_i$, I is the intensity, and K is some constant of proportionality. It was found by Medvedev et al. (2016) that at high Δ_v, this relationship can be broken resulting in an unphysical flattening, and even an increase of the intensity. They identify that the primary culprit in this situation is the numerical noise added by the aforementioned interpolation. Hence, the representation of the dipole is an important aspect in physical modelling. The method suggested

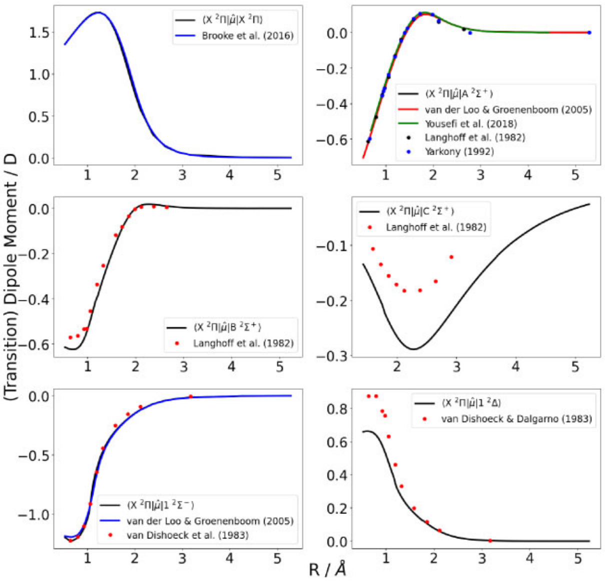

Figure 15. Comparison of *ab initio* (T)DMCs from this work and those from (Langhoff et al. 1982; van Dishoeck et al. 1983; van Dishoeck & Dalgarno 1983; van der Loo & Groenenboom 2005; Brooke et al. 2016; Yousefi et al. 2018).

in this work is to represent the dipole not as grid points, and instead to find an analytic representation. Medvedev & Ushakov (2022) suggested the *irregular DMC* form as in equation (41) which is fitted to the *ab initio* grid points to produce an analytical representation of the *ab initio* dipole moment as given by

$$D(R) = \chi(R; c_2, ..., c_6) \sum_{i=0}^{6} b_i T_i(z(R)), \tag{41}$$

$$\chi(R; c_2, ..., c_6) = \frac{\left(1-\mathrm{e}^{-c_2 R}\right)^3}{\sqrt{\left(R^2-c_3^2\right)^2+c_4^2\sqrt{\left(R^2-c_5^2\right)^2+c_6^2}}}, \tag{42}$$

$$z(R) = 1 - 2\mathrm{e}^{-c_1 R}, \tag{43}$$

where T_i are the Chebyshev polynomials of the first kind. b_i and c_i are variable parameters. This form was successfully used by Brady et al. (2023) to produce such a representation for the ground state permanent dipole of SO. Medvedev et al. (2024) found that the intensities past $\Delta_v \geq 6$ from Brooke et al. (2016) are unreliable due to the aforementioned intensity flattening. To test this, intensities are calculated using the original grid point representation from this work, the grid point representation from Brooke et al. (2016), and analytic representations of both curves, and are examined. Fig. 16 presents the grid point and analytic representations of these dipoles along with their fit residuals. Intensities are then computed and plotted in chunks covering a single Δ_v, the maximum of each subset is then found and equation (40) is fit to these points. The resulting R^2 value. Equation (44) is measured by fitting between $v = 0$ and 12.

$$R^2 = 1 - \frac{\sum_i \left(\hat{\mu}_i^{\text{grid}} - \hat{\mu}_i^{\text{fitted}}\right)^2}{\sum_i \left(\hat{\mu}_i^{\text{grid}} - \left\langle \hat{\mu}_i^{\text{grid}} \right\rangle\right)^2}. \tag{44}$$

From Fig. 17, it appears that the dipole from Brooke et al. (2016) is not appropriate for modelling transitions with $\Delta_v > 7 \rightarrow 9$, a similar conclusion to that of Medvedev et al. (2024). The grid point representation returns unphysical intensities at $\Delta_v = 9$. Fitting the dipole returns an unphysical intensity at $\Delta_v = 7$, however, which is unexpected. Fitting an analytic representation of the dipole is challenging, and the best fit for this dipole returned an RMS of the order of 10^{-4}. This is likely an insufficient accuracy for modelling these intensities. The *ab initio* dipole from this work returned better results, with intensities obeying equation (40) up to $\Delta_v = 11$ for the grid point representation and $\Delta_v = 12$ for the analytic representation, with a fit RMS of the order of 10^{-5}. In this work, the fitted *ab initio* dipole was hence chosen to model the intensities and Meinel band transitions with $\Delta v > 12$ are removed.

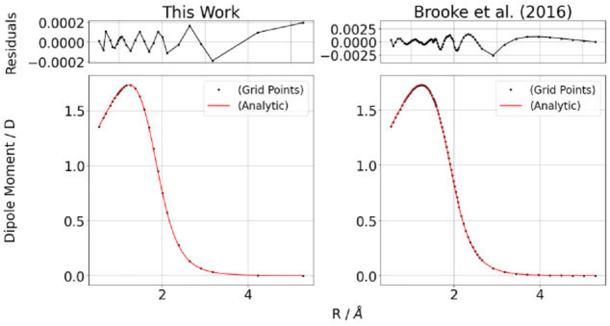

Figure 16. Grid point and analytic representations of the X–X permanent dipole moment of OH. Left panel: this work. Right panel: Brooke et al. (2016).

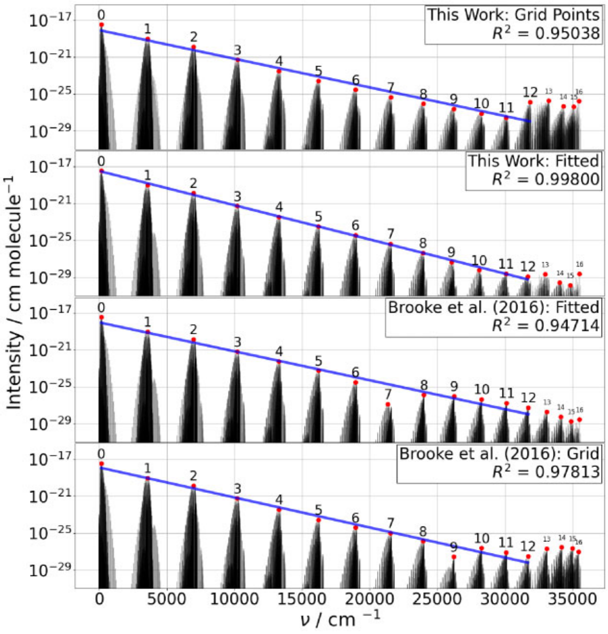

Figure 17. Hydroxyl ground-to-ground transitions with different representation of the ground state permanent dipole. Dipoles from section 2 and Brooke et al. (2016). Numbers represent Δ_v. Dots are maxima for given Δ_v. Straight line is a fitted linear relationship through points with $\Delta_v \leq 12$.

Recently, Chang et al. (2023) measured experimental line intensities for the P-branch rovibrational transitions in X $^2\Pi$ for the $v'' \rightarrow v'' = 0 \rightarrow 1$ vibrational band, reporting that the intensities of the HITRAN line list are ~ 1.4 times stronger than their measured intensities. These transition intensities were compared with the corresponding calculated intensities from this work and it was found that agreement with HITRAN is conserved. The HITRAN intensity uncertainties for OH are all ≥ 10 per cent, and an average of ~ 5 per cent difference is found between the MYTHOS and HITRAN intensities is found, with all lines agreeing within uncertainty. Disagreement is found between MYTHOS and the recently

Table 10. Comparison between calculated (MYTHOS) line intensities in the X $^2\Pi$ state $v'' \rightarrow v'' = 0 \rightarrow 1$ vibrational band and their HITRAN (Gordon et al. 2022) and measured (Chang et al. 2023) counterparts. Percentage differences are calculated as $\Delta = (I_{\rm MYTHOS} - I_{\rm Reference})/(I_{\rm Reference}) \times 100$. $\langle\Delta\rangle$ is the average percentage difference.

	Quantum numbers		Line Intensities/cm molecule^{-1} $\times\ 10^{-20}$			Δ/ per cent	
Branch	computed by including	e/f'	MYTHOS	HITRAN	Measured	HITRAN	Measured
P	2.5	e	5.93	5.60	4.15	5.85 per cent	42.84 per cent
P	2.5	e	3.29	3.14	2.41	4.86 per cent	36.62 per cent
P	2.5	f	5.86	5.59	4.15	4.78 per cent	41.13 per cent
P	2.5	f	3.30	3.14	2.41	5.11 per cent	36.94 per cent
P	3.5	f	2.69	2.54	1.91	5.94 per cent	40.89 per cent
P	3.5	e	2.66	2.55	1.91	4.38 per cent	39.36 per cent
P	4.5	e	4.89	4.56	3.38	7.14 per cent	44.55 per cent
P	4.5	e	1.60	1.54	1.09	4.09 per cent	47.07 per cent
P	4.5	f	4.74	4.54	3.38	4.37 per cent	40.19 per cent
P	4.5	f	1.63	1.54	1.09	6.16 per cent	49.98 per cent
					$\langle\Delta\rangle$	5.27 per cent	41.96 per cent

measured lines of Chang et al. (2023), with our intensities being around 40 per cent higher, see Table 10.

While this discrepancy is troubling, it does not provide sufficient evidence to scale the current dipoles in the model as the measured values only cover a narrow slice in J and v, furthermore, Chang et al. (2023) only consider one branch of transitions. It is not known if such a similar trend is followed by other rovibrational transitions, and so, for the time being, the dipole model is left as is.

6.2 Partition function

The temperature-dependent partition function for OH was calculated as the sum from equation (33). For convenience, the equation is rewritten as follows:

$$Q(T) = \sum_n g_n^{\rm tot} {\rm e}^{-c_2 E_n/T}. \tag{45}$$

As $Q(T)$ is expressed as a sum over J, the value of $Q(T)$ at some T depends on the value of $J_{\rm max}$. To ensure completeness of the line list, it is a requirement that, up to a given temperature, in the case of this line list, 8000 K, the value of $Q(T = 8000)$ converges with $J_{\rm max}$. In order to test this convergence against $J_{\rm max}$, one can study how the value $J_{\rm max}$ impacts the value of $Q(T)$. Defining $Q(T; J_{\rm max})$ as $Q(T)$ computed by including only states with $J_n \leq J_{\rm max}$.

We define the difference $\Delta_Q(T, J_{\rm max})$ as follows:

$$\Delta_Q(T, J_{\rm max}) = Q(T; J_{\rm max}) - Q(T; J_{\rm max} - 1). \tag{46}$$

In this study, the rotational basis is set to a maximum $J_{\rm max} = 49.5$. An estimate for the convergence, Δ_Q is hence given by

$$\Delta_Q(T) = 1 - \frac{\Delta_Q(T, J_{\rm max})}{Q(T; J_{\rm max} - 1)}. \tag{47}$$

A visualization of this is presented in Fig. 18, where it is clear that up to 10 000 K, there is a good level of convergence and $\Delta_Q(T = 10\,000) = 99.87$ per cent.

The JPL database (Pickett et al. 1998) provides partition function values up to $T = 300$ K. Barklem & Collet (2016) provide numerical values for the partition functions of OH up to 10 000 K which have been multiplied by 2 to account for difference treatments of the nuclear spin degeneracy, which for OH has a value of $g_{\rm ns} = 2$. Sauval & Tatum (1984) provide a polynomial expansion form of the partition function of OH which they claim is good between 1000 and 9000 K. The polynomial takes the form:

$$\log_{10} Q(T) = \sum_0^{n_{\rm max}} a_n \log_{10}(5040/T)^n. \tag{48}$$

a_n here is given up to $n = 3$. Again, the results of this polynomial have been multiplied by 2 to account for the nuclear spin degeneracy. Fig. 19 presents a comparison between this work and the sources listed above. There is good agreement with Pickett et al. (1998) at all temperatures, however, our results are slightly higher as we have a larger vibrational basis and more electronic states. We return good agreement with HITRAN (Gamache et al. 2017).

For lower temperatures, there is poor agreement with Barklem & Collet (2016) and Sauval & Tatum (1984) and good agreement is returned at higher temperatures. The values from these sources are based on calculated, rather than experimental molecular constants from Huber & Herzberg (1979), however, and we believe that our partition function in this region is correct as the energy levels from this work's model have been supplemented with the MARVEL energy levels from Furtenbacher et al. (2022) as per the procedures by Bowesman et al. (2021, 2024), and McKemmish et al. (2024).

6.3 Line list and bound-to-bound transitions

DUO was used to produce an OH line list which is called MYTHOS and is part of the ExoMol 2024 data release (Tennyson et al. 2024). This line list is given in the ExoMol format (Tennyson et al. 2014, 2020) according to the latest standards (Tennyson et al. 2023). In this standard we include the predissociation lifetimes convoluted with the radiative lifetime as per equation (38).

The line list contains 10 606 rovibronic bound and quasi-bound states and 1268 570 dipole allowed X–X, A–A, B–B, C–C, and X–ABC transitions between bound–bound and bound–quasi-bound states, comprising the ExoMol line list .STATES and .TRANS files.

Before the procedure in Section 4, 58 289 states and 47 419 460 transitions were calculated, the identified continuum states and transitions are used in the continuum absorption cross-sections (.CONT files) alongside the transitions from X $^2\Pi$ to 1 $^2\Sigma^-$ and 1 $^2\Delta$.

Furthermore, this data set is, wherever possible, supplemented with the MARVEL energy levels from Furtenbacher et al. (2022), including calculated and interpolated levels and uncertainties as per the hybridization procedure.

In line with current standards, the last two columns in the .STATES file are 'Type' indicating whether a state has the MARVEL

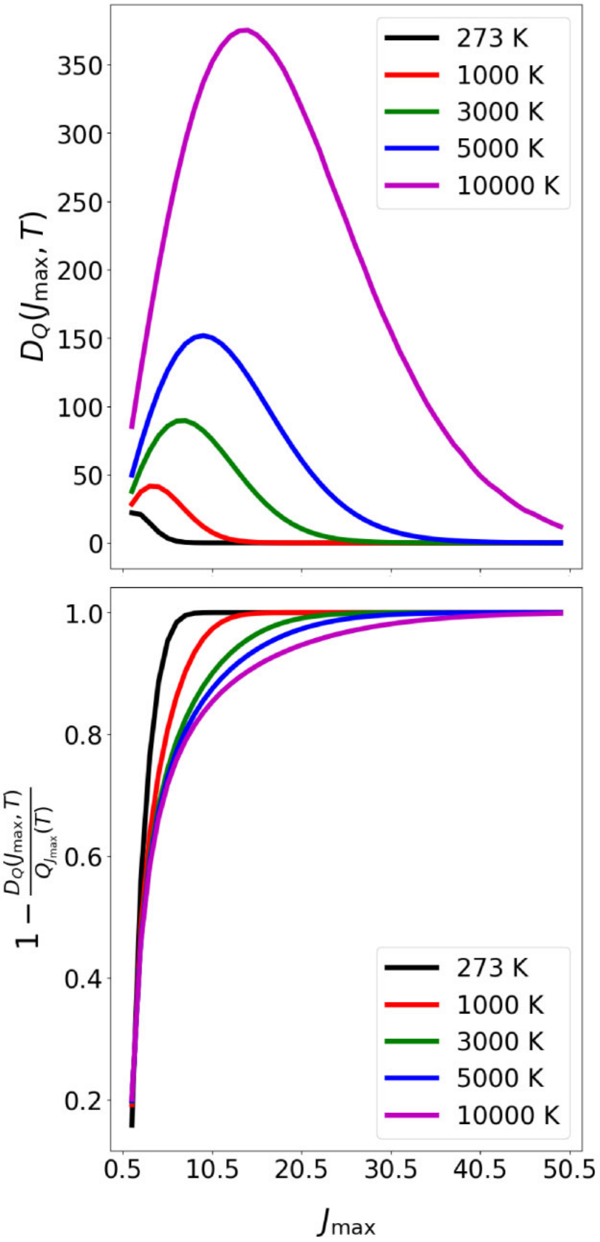

Figure 18. Convergence of the partition function of OH as a function of $J_{\max}$.

energy (Ma), calculated from the spectroscopic model (Ca), or been produced from the PSs algorithm (Bowesman et al. 2021, 2024; McKemmish et al. 2024) and E_{Calc}, giving the calculated energy, which, in cases that Type is Ca, would be equal to the energy column, E. A sample from the .STATES file is given in Table 11. Similarly, an extract of the .TRANS file is given in Table 12.

6.4 Simulation of absorption spectrum

The absorption spectrum of OH is simulated in two parts, bound–bound/quasibound transitions which are broadened appropriately using Voigt profiles, and the bound–unbound continuum absorption transition which are discussed in more detail by Mitev et al. (in preparation). The cross-sections are computed using PYEXOCROSS (Zhang, Tennyson & Yurchenko 2024) and for the two cases the calculations are done independently and then added together afterwards.

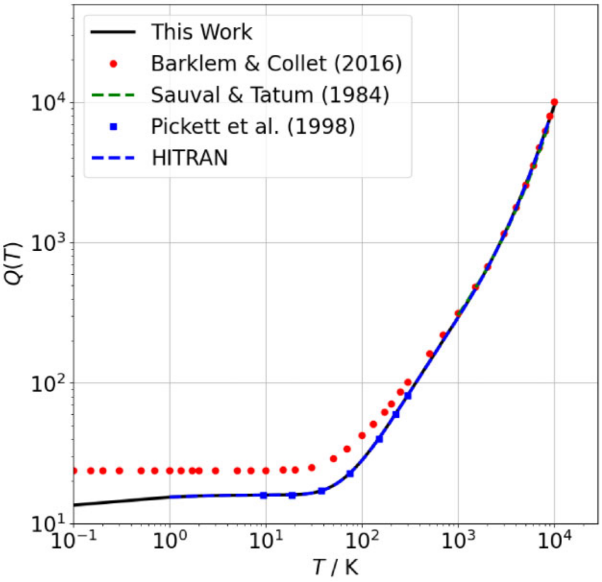

Figure 19. Comparison of partition function between this work and Barklem & Collet (2016), Sauval & Tatum (1984), Pickett et al. (1998), and Gordon et al. (2022).

A comparison between the transition stick spectra of this work and the available spectra from HITRAN is given in Fig. 20. This reference line list from HITRAN (Gordon et al. 2022) is based on the available MoLLIST data (Yousefi et al. 2018). The MYTHOS line list extends the X–A transitions and provides previously unavailable transitions to the B and C states. Where quantum numbers coincide, there is good agreement on position and intensity. Transition frequencies above 80 000 cm^{-1} are not included in the line list due to poor agreement with available cross-section data (see Fig. 22 and discussion). However, transitions to the C $^2\Sigma^+$ state from high v X $^2\Pi$ states are still included and are visible at high temperatures as hot bands. The full photoabsorption cross-section is simulated by applying a Voigt profile to all bound–bound transitions to include their lifetime, Doppler, and pressure-broadening effects.

In addition, the aforementioned continuum absorption cross-sections are included. These cover transitions between the X $^2\Pi$ state and the unbound regions of A $^2\Sigma^+$, B $^2\Sigma^+$ (Section 4), 1 $^2\Sigma^-$, and 1 $^2\Delta$. .CONT files are given for a specific temperature, T for $T \in [100, 200, ..., 8000]$ K, 0 bar of pressure, and in steps of 0.01 cm^{-1}. Examples of the complete photoabsorption cross-section are given for $T \in [300, 1000, 2000, 5000]$ K in Fig. 21. The Leiden database (Hrodmarsson & van Dishoeck 2023) provides photoabsorption cross-sections for OH. These cross-sections do not consider temperature and so are assumed to be at low T. A 1 K calculation is produced and Fig. 22 presents a comparison between the cross-sections from this work and from Leiden. It appears that the reference material does not consider much of the lower energy regions covered by rovibrational transitions in X $^2\Pi$ and misses much of the predissociation structure of the A $^2\Sigma^+$ state. Otherwise, there appears to be a good agreement in the continuum absorption region, except for the small 'bump' around 55 000 cm^{-1}. It is not certain what this is caused by. Above 80 000 cm^{-1} agreement is poor, this is because the model in this work fails to include the effects caused by higher energy Rydberg states which had not been included in the MARVEL data set (Furtenbacher et al. 2022) such as the 2 $^2\Pi$, 3 $^2\Pi$,

Table 11. Sample of the .STATES file produced by DUO for OH. Uncertainties using PSs procedure from Bowesman et al. (2021, 2024), McKemmish et al. (2024), lifetimes are convolutions of predissociative and radiative lifetimes (Paper I), and Landé g factors, (g_L) are produced using DUO as per Semenov, Yurchenko & Tennyson (2017).

n	E	g^{tot}	J	Δ	τ	g_L	$+/-$	e/f	State	v	Λ	Σ	Ω	Type	E_{Calc}
1	126.292 196	4	0.5	0.001 000	28.5630	−0.000 755	+	e	X(2PI)	0	1	−0.5	0.5	Ma	126.252 576
2	3695.355 577	4	0.5	0.001 118	0.0565	−0.000 755	+	e	X(2PI)	1	1	−0.5	0.5	Ma	3695.476 889
3	7098.826 455	4	0.5	0.001 118	0.0300	−0.000 755	+	e	X(2PI)	2	1	−0.5	0.5	Ma	7098.923 205
4	10 338.617 460	4	0.5	0.001 225	0.0206	−0.000 754	+	e	X(2PI)	3	1	−0.5	0.5	Ma	10 338.753 725
5	13 415.819 989	4	0.5	0.001 225	0.0154	−0.000 754	+	e	X(2PI)	4	1	−0.5	0.5	Ma	13 416.012 960
6	16 330.523 242	4	0.5	0.001 225	0.0119	−0.000 754	+	e	X(2PI)	5	1	−0.5	0.5	Ma	16 330.622 842
7	19 081.594 976	4	0.5	0.001 225	0.0094	−0.000 754	+	e	X(2PI)	6	1	−0.5	0.5	Ma	19 081.510 489
8	21 666.391 134	4	0.5	0.001 225	0.0075	−0.000 753	+	e	X(2PI)	7	1	−0.5	0.5	Ma	21 666.224 458
9	24 080.351 827	4	0.5	0.001 225	0.0061	−0.000 753	+	e	X(2PI)	8	1	−0.5	0.5	Ma	24 080.302 420
10	26 316.481 722	4	0.5	0.001 225	0.0051	−0.000 753	+	e	X(2PI)	9	1	−0.5	0.5	Ma	26 316.585 759

Notes. n: state counting number.
E: state energy in cm^{-1}.
g^{tot}: total degeneracy of the state.
J: angular momentum quantum number.
Δ: energy level uncertainty in cm^{-1}.
τ: lifetime of the state in seconds.
g_L: Landé g factor (Semenov et al. 2017).
$+/-$: parity.
e/f: rotationless parity.
State: electronic state, X(2PI), A(2SIGMA+), B(2SIGMA+), or C(2SIGMA +).
v: vibrational quantum number.
Λ: projection of electronic angular momentum.
Σ: projection of electronic spin.
Ω: $\Lambda + \Sigma$ (Projection of total electron angular momentum).
Type: Ma – marvelized, Ca – calculated, PS – predicted shifts interpolation.
E_{Calc}: calculated DUO energy directly from spectroscopic model.

Table 12. Sample of the .TRANS file produced by DUO for OH.

n_f	n_i	A (s^{-1})	ν (cm^{-1})
1114	988	6.4725E-17	0.001 643
636	510	1.1482E-16	0.002 989
254	381	1.9358E-15	0.003 251
1268	1394	5.8108E-17	0.004 522
252	379	2.8534E-14	0.006 179
1385	1259	1.4371E-15	0.006 428
763	890	5.7538E-16	0.006 531
1261	1387	1.8765E-15	0.007 636
250	377	1.5369E-13	0.009 289
1142	1016	1.2792E-15	0.010 669

and D $^2\Sigma^-$ states. Therefore, both the ExoMol line list (.STATES and .TRANS) and the continuum absorption cross-sections (.CONT) are truncated to include only transitions of frequency $< 80\,000$ cm^{-1}.

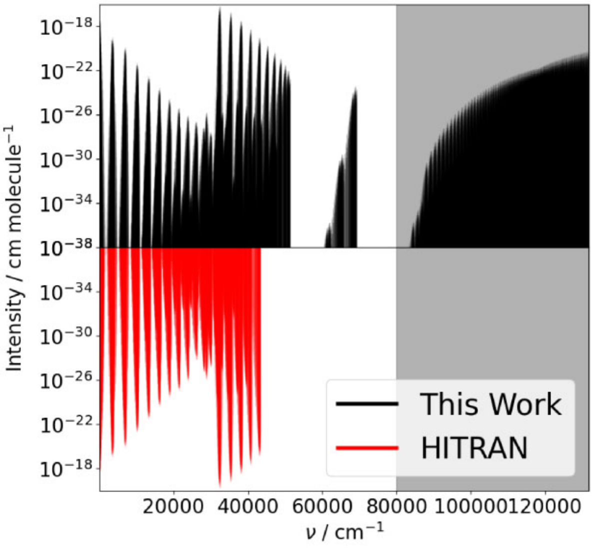

Figure 20. Comparison of stick spectra produced with ^{16}O^{1}H MYTHOS line list and the HITRAN line list (Gordon et al. 2022) at 296 K. Wavenumbers above 80 000 cm^{-1} are not included in the MYTHOS line list.

7 CONCLUSIONS AND FUTURE WORK

A new OH line list called MYTHOS is presented covering regions up to 80 000 cm^{-1} in energy (>125 nm in wavelength). *Ab initio* electronic structure calculations of eight electronic states have been performed covering these states' PECs, corresponding diagonal/off-diagonal coupling curves, and (transition) dipole moment curves (Section 2). This *ab initio* study was heavily influenced by the works of van der Loo & Groenenboom (2005), who provided optimal CAS-SCF active spaces for use in MOLPRO.

The line list's constituent files contain all bound states and bound–bound transitions, ideally with little or no excess unbound lines. To achieve this, a framework for identifying bound and unbound states was explored, leveraging the close-to-boundary regions of the wavefunctions of individual states; this leads to bound–bound (line list) and bound–unbound (.CONT) data sets.

Temperature-dependent photoabsorption spectra for $T \in [1, 300, 1000, 2000, 5000]$ K are presented in Figs 21 and 22, with good agreement with the available Leiden data set (Hrodmarsson & van Dishoeck 2023) up to 80 000 cm^{-1} (∼125 nm) at 1 K. The photoabsorption cross-section presented here

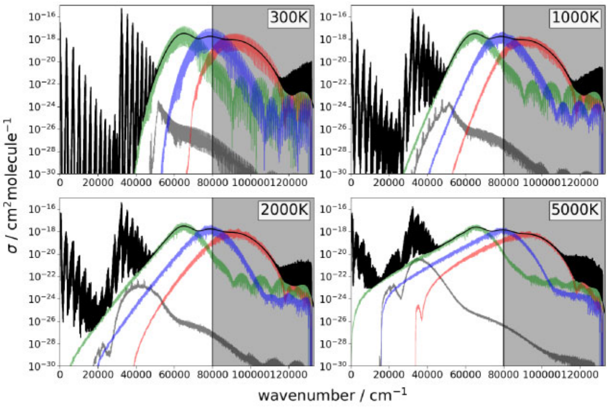

Figure 21. Computed temperature dependent photoabsorption cross-sections of the transitions of OH for varying temperature. Shaded regions are not provided in supplementary material, see the text.

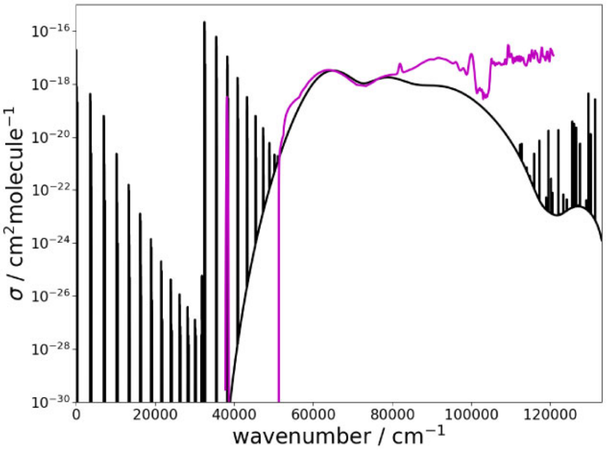

Figure 22. Comparison between the photoabsorption cross-section of OH computed in this work (darker line) at 1 K and cross-section given by Leiden database (Hrodmarsson & van Dishoeck 2023) (lighter line).

provides more information on the structure of transitions below $\sim 50\,000\,\mathrm{cm}^{-1}\,(\gtrsim 200\,\mathrm{nm})$, including rovibrational transitions in X $^2\Pi$ and a complete description of the predissociative transitions of $A^2\Sigma^+ \leftarrow X^2\Pi$. Continuum absorption effects above $\sim 50\,000$ $\mathrm{cm}^{-1}\,(\lesssim 200\,\mathrm{nm})$ stem from transitions from the X $^2\Pi$ state to the 1 $^2\Sigma^-$ 1 $^2\Delta$, A $^2\Sigma^+$, and B $^2\Sigma^+$ states.

Above $80\,000\,\mathrm{cm}^{-1}$, one must consider the effects of multiple other states to properly model the spectrum. These states include, but are not limited to the 2 $^2\Pi$, 3 $^2\Pi$, and D $^2\Sigma^-$ states. These electronic states have been studied by van Dishoeck et al. (1984), van Dishoeck & Dalgarno (1984b) and are known to be important sources of dissociation for OH above $80\,000\,\mathrm{cm}^{-1}$ through direct continuum absorption from X $^2\Pi \rightarrow$ 2 $^2\Pi$, predissociation to the 2 $^2\Pi$ state from B $^2\Sigma^+$, 3 $^2\Pi$, C $^2\Sigma^+$, and D $^2\Sigma^-$, and spontaneous radiative decay from D $^2\Sigma^-$ (van Dishoeck & Dalgarno 1984b; Greenslade et al. 2005; van der Loo & Groenenboom 2005). Performing further, high-quality electronic structure calculations to cover some of these states, and modelling their spectra including their dissociative mechanisms has hence been left as future work.

For the time being, however, this model extends the current ExoMol and HITRAN OH line list higher in energy by $\sim 35\,000\,\mathrm{cm}^{-1}$, and produces a photoabsorption spectrum with good agreement with the reference material.

ACKNOWLEDGEMENTS

We thank Tibor Furtenbacher and Attila Császár for their work producing the MARVEL data set used in this work. We acknowledge the use of the UCL Myriad High Performance Computing Facility (Myriad@UCL), and associated support services, in the completion of this work. This work was supported by ERC Advanced Investigator Project 883830 and by UK STFC under grant ST/Y001508/1.

DATA AVAILABILITY

The ^{16}O^{1}H MYTHOS DUO input (.INP), .STATES, .TRANS, .CONT, and partition function (.PF) files can be downloaded from www.exomol.com. A $^2\Sigma^+$ state predissociation lifetimes are given as supplementary material to this article.

The open-access programs DUO, EXOCROSS, and PYEXOCROSS are available from github.com/exomol.

REFERENCES

Barklem P. S., Collet R., 2016, A&A, 588, A96
Bauschlicher C. W. Jr, Langhoff S. R., 1987, J. Chem. Phys., 87, 4665
Berdyugina S. V., Solanki S. K., 2001, A&A, 380, L5
Bernath P. F., 2020, J. Quant. Spectrosc. Rad. Trans., 240, 106687
Bernath P. F., Colin R., 2009, J. Mol. Spectrosc., 257, 20
Bowesman C. A., Shuai M., Yurchenko S. N., Tennyson J., 2021, MNRAS, 508, 3181
Bowesman C. A., Qu Q., McKemmish L. K., Yurchenko S. N., Tennyson J., 2024, MNRAS, 529, 1321
Brady R. P., Yurchenko S. N., Tennyson J., Kim G.-S., 2023, MNRAS, 527, 6675
Brasseur G., Offermann D., 1986, J. Geophys. Res.-Atmos., 91, 10818
Brooke J. S. A., Bernath P. F., Western C. M., Sneden C., Afsar M., Li G., Gordon I. E., 2016, J. Quant. Spectrosc. Radiat. Transf., 168, 142
Brown J. M., Cheung A. S. C., Merer A. J., 1987, J. Mol. Spectrosc., 124, 464
Chang C.-W., Chen I.-Y., Fittschen C., Luo P.-L., 2023, J. Chem. Phys., 159, 184203
Chen Q., Hu X., Guo H., Xie D., 2021, J. Phys. Chem. Lett., 12, 1822
Clancy R. T. et al., 2013, Icarus, 226, 272
Colin R., Coheur P. F., Kiseleva M., Vandaele A. C., Bernath P. F., 2002, J. Mol. Spectrosc., 214, 225
Coxon J. A., Sappey A. D., Copeland R. A., 1991, J. Mol. Spectrosc., 145, 41
Franzen C., Espy P. J., Hofmann N., Hibbins R. E., Djupvik A. A., 2019, Atmosphere, 10, 637
Furtenbacher T., Hegedus S. T., Tennyson J., Császár A. G., 2022, Phys. Chem. Chem. Phys., 24, 19287
Gamache R. R. et al., 2017, J. Quant. Spectrosc. Radiat. Transf., 203, 70
Garmash O. et al., 2020, Atmos. Chem. Phys., 20, 515
Gordon I. et al., 2022, J. Quant. Spectrosc. Radiat. Transf., 277, 107949
Gould T., Bucko T., 2016, J. Chem. Theory Comput., 12, 3603
Greenslade M. E., Lester M. I., Radenović D. C., van Roij A. J. A., Parker D. H., 2005, J. Chem. Phys., 123, 074309
Herbig G. H., 1974, ApJ, 189, 75
Herzberg G., 1989, Molecular Spectra and Molecular Structure I. Spectra of Diatomic Molecules. Krieger Publication, Melbourne, FL, p. 223
Hrodmarsson H. R., van Dishoeck E. F., 2023, A&A, 675, A25
Huber K. P., Herzberg G., 1979, Molecular Spectra and Molecular Structure IV. Constants of Diatomic Molecules. Van Nostrand Reinhold Company. New York, NY
Hwang E. S., Lipson J. B., Field R. W., Dodd J. A., 2001, J. Phys. Chem. A, 105, 6030

Joens J. A., 2001, J. Phys. Chem. A, 105, 11041

Jones T. J., Hyland A. R., Fix J. D., Cobb M. L., 1988, AJ, 95, 158

Kaufmann M., Lehmann C., Hoffmann L., Funke B., López-Puertas M., Savigny C., Riese M., 2008, Adv. Space Res., 41, 1914

Kozin I. N., Roberts R. M., Tennyson J., 1999, J. Chem. Phys., 111, 140

Kozlov S. V., Pazyuk E. A., Stolyarov A. V., 2024, Russ. J. Phys. Chem. A, 98, 897

Kramida A., Ralchenko Y., Reader J., ASD NIST, 2021, NIST Atomic Spectra Database (ver. 5.9). National Institute of Standards and Technology, Gaithersburg, MD, available at: http://physics.nist.gov/asd [Accessed October 2021]

Kristiansson M. K. et al., 2022, Nat. Commun., 13, 5906

Landman R., Sanchez-Lopez A., Molliere P., Kesseli A. Y., Louca A. J., Snellen I. A. G., 2021, A&A, 656, A119

Langhoff S. R., Davidson E. R., 1974, Int. J. Quant. Chem., 8, 61

Langhoff S. R., van Dishoeck E. F., Wetmore R., Dalgarno A., 1982, J. Chem. Phys., 77, 1379

Le Roy R. J., Henderson R. D. E., 2007, Mol. Phys., 105, 663

Le Roy R. J., Dattani N. S., Coxon J. A., Ross A. J., Crozet P., Linton C., 2009, J. Chem. Phys., 131, 204309

Le Roy R. J., Haugen C. C., Tao J., Li H., 2011, Mol. Phys., 109, 435

Lee E. G., Seto J. Y., Hirao T., Bernath P. F., Le Roy R. J., 1999, J. Mol. Spectrosc., 194, 197

Le Roy R. J., 2017, J. Quant. Spectrosc. Radiat. Transf., 186, 179

Le Roy R. J., Huang Y., Jary C., 2006, J. Chem. Phys., 125, 164310

McKemmish L. K., Bowesman C. A., Kefala K., Perri A. N., Syme A. M., Yurchenko S. N., Tennyson J., 2024, RAS Tech. Instr., 3, 565

Medvedev E. S., Ushakov V. G., 2022, J. Quant. Spectrosc. Rad. Trans., 288, 108255

Medvedev E. S., Meshkov V. V., Stolyarov A. V., Ushakov V. G., Gordon I. E., 2016, J. Mol. Spectrosc., 330, 36

Medvedev E. S., Ermilov A. Y., Ushakov V. G., 2024, Mol. Phys., 0, e2395439

Meinel I. A. B., 1950, ApJ, 111, 555

Meuwly M., Hutson J. M., 1999, J. Chem. Phys., 110, 8338

Mitev G. B., 2024, Phd thesis, Univ. College London (UCL), London

Mitev G. B., Taylor S., Tennyson J., Yurchenko S. N., Buchachenko A. A., Stolyarov A. V., 2022, MNRAS, 511, 2349

Mitev G. B., Yurchenko S. N., Tennyson J., 2024, J. Chem. Phys., 160, 144110 (Paper I)

Munoz-Romero C. E. et al., 2024, ApJ, 964, 36

Nugroho S. K. et al., 2021, ApJ, 910, L9

Patrascu A. T., Hill C., Tennyson J., Yurchenko S. N., 2014, J. Chem. Phys., 141, 144312

Pezzella M., Yurchenko S. N., Tennyson J., 2021, Phys. Chem. Chem. Phys., 23, 16390

Pezzella M., Yurchenko S. N., Tennyson J., 2022, MNRAS, 514, 4413

Pezzella M., Mitev G., Yurchenko S. N., Tennyson J., Mitrushchenkov A. O., 2024, Phys. Chem. Chem. Phys., 26, 27519

Piccioni G. et al., 2008, A&A, 483, L29

Pickett H. M., Poynter R. L., Cohen E. A., Delitsky M. L., Pearson J. C., Müller H. S. P., 1998, J. Quant. Spectrosc. Radiat. Transf., 60, 883

Prinn R. G. et al., 1995, Science, 269, 187

Qin X., Zhang S. D., 2014, J. Korean. Phys. Soc., 65, 2017

Sappey A. D., Crosley D. R., Copeland R. A., 1989, J. Chem. Phys., 90, 3484

Sauval A. J., Tatum J. B., 1984, ApJS, 56, 193

Scheidegger S., Merkt F., 2024, Phys. Rev. Lett., 132, 113001

Semenov M., Yurchenko S. N., Tennyson J., 2017, J. Mol. Spectrosc., 330, 57

Skokov S., Peterson K. A., Bowman J. M., 1999, Chem. Phys. Lett., 312, 494

Srivastava S., Sathyamurthy N., 2014, J. Phys. Chem. A, 118, 6343

Sulakshina O. N., Borkov Y. G., 2023, Mol. Phys., 121, e2222346

Sun G., Zheng X.-F., Qin Y., Song Y., Zhang J., Amero J. M., Vázquez G. J., 2020, Chin. J. Chem. Phys., 33, 129

Šurkus A. A., Rakauskas R. J., Bolotin A. B., 1984, Chem. Phys. Lett., 105, 291

Tang K. T., 1969, Phys. Rev., 177, 108

Tennyson J., Hill C., Yurchenko S. N., 2013, AIP 6th Int. Conf. On Atomic and Molecular Data and Their Applications ICAMDATA-2012. Am. Inst. Phys., New York, p. 186

Tennyson J. et al., 2014, Pure Appl. Chem., 86, 1931

Tennyson J., Lodi L., McKemmish L. K., Yurchenko S. N., 2016, J. Phys. B-At. Mol. Opt. Phys., 49, 102001

Tennyson J. et al., 2020, J. Quant. Spectrosc. Radiat. Transf., 255, 107228

Tennyson J., Pezzella M., Zhang J., Yurchenko S. N., 2023, RAS Tech. Instr., 2, 231

Tennyson J. et al., 2024, J. Quant. Spectrosc. Radiat. Transf., 326, 109083

van Dishoeck E. F., Dalgarno A., 1983, J. Chem. Phys., 79, 873

van Dishoeck E. F., Dalgarno A., 1984a, Icarus, 59, 305

van Dishoeck E. F., Dalgarno A., 1984b, ApJ, 277, 576

van Dishoeck E. F., Langhoff S. R., Dalgarno A., 1983, J. Chem. Phys., 78, 4552

van Dishoeck E. F., van Hemert M. C., Allison A. C., Dalgarno A., 1984, J. Chem. Phys., 81, 5709

van der Loo M. P. J., Groenenboom G. C., 2005, J. Chem. Phys., 123, 074310

Weinreb S., Barrett A. H., Henry J. C., Meeks M. L., 1963, Nature, 200, 829

Werner H.-J., Knowles P. J., 1985, J. Chem. Phys., 82, 5053

Werner H. J., Knowles P. J., Lindh R., Manby F. R., Schütz M., 2010, MOLPRO, a package of ab initio programs, available at: https://www.molpro.net [Accessed December 2024]

Werner H.-J., Knowles P. J., Knizia G., Manby F. R., Schütz M., 2012, WIREs Comput. Mol. Sci., 2, 242

Werner H.-J. et al., 2020, J. Chem. Phys., 152, 144107

Western C. M., 2017, J. Quant. Spectrosc. Radiat. Transf., 186, 221

Yarkony D. R., 1992, J. Chem. Phys., 97, 1838

Yousefi M., Bernath P. F., Hodges J., Masseron T., 2018, J. Quant. Spectrosc. Radiat. Transf., 217, 416

Yurchenko S. N., Lodi L., Tennyson J., Stolyarov A. V., 2016, Comput. Phys. Commun., 202, 262

Yurchenko S. N., Al-Refaie A. F., Tennyson J., 2018, A&A, 614, A131

Yurchenko S. N., Szajna W., Hakalla R., Semenov M., Sokolov A., Tennyson J., Pavlenko Y., Schmidt M. R., 2024, MNRAS, 527, 9736

Zannese M., Tabone B., Habart E., Le Petit F., van Dishoeck E. F., Bron E., 2023, A&A, 671, A41

Zhang J., Tennyson J., Yurchenko S. N., 2024, RAS Tech. Instr., 3, 257

SUPPORTING INFORMATION

Supplementary data are available at *MNRAS* online.

PREDISSOCIATION_LIFETIMES_A(2SIGMA+).txt

Please note: Oxford University Press is not responsible for the content or functionality of any supporting materials supplied by the authors. Any queries (other than missing material) should be directed to the corresponding author for the article.

This paper has been typeset from a TEX/LATEX file prepared by the author.